AGU ADVANCING EARTH AND SPACE SCIENCES

Water Resources Research

RESEARCH ARTICLE
10.1029/2025WR040217

Experimental and Numerical Investigation on the Impact of Emergent Vegetation on the Hyporheic Exchange

S. H. Huang[1,2,3], R. Nuli[1,4], P. K. Kang[1,5], L. Shen[1,4], and J. Q. Yang[1,2]

[1]Saint Anthony Falls Laboratory, University of Minnesota, Minneapolis, MN, USA, [2]Department of Civil, Environmental, and Geo- Engineering, University of Minnesota, Minneapolis, MN, USA, [3]Department of Civil Engineering, National Taiwan University, Taipei, Taiwan, [4]Department of Mechanical Engineering, University of Minnesota, Minneapolis, MN, USA, [5]Department of Earth and Environmental Sciences, University of Minnesota, Minneapolis, MN, USA

Abstract Hyporheic exchange leads to the transfer of gases, solutes, and fine particles across the sediment-water interface, playing a critical role in biogeochemical cycles and pollutant transport in aquatic environments. While in-channel vegetation has been recognized to enhance hyporheic exchange, the mechanisms remain poorly understood. Here, we investigated how an emergent vegetation canopy impacts hyporheic exchange using refractive index-matched flume experiments and coupled numerical simulations. Our results show that at the same mean surface flow velocity, vegetation increases the hyporheic exchange velocity by four times compared to the non-vegetated channel. However, the hyporheic exchange velocity does not increase further with increasing vegetation density. In addition, our results show that the hyporheic exchange velocity scales with the square root of sediment permeability. Our findings provide a predictive framework for hyporheic exchange in vegetated channels with varying vegetation densities and sediment permeabilities and could guide the future design of environmental management and restoration projects using vegetation.

Plain Language Summary Aquatic vegetation is known to increase hyporheic exchange, which facilitates the exchange of gases, solutes, and fine particles between surface water and pore fluids within the sediment beds. Due to its ability to regulate the fate of pollutants, vegetation has been used to remediate contamination in many riverine and coastal restoration projects. However, the mechanisms through which vegetation enhances hyporheic exchange remain poorly understood, making it challenging for engineers to design effective restoration projects. In this study, we investigated how an emergent vegetation canopy impacts hyporheic exchange using both laboratory experiments and numerical simulations. Our results showed that at the same mean surface flow velocity, hyporheic exchange was four times faster in the vegetated channel than in a channel without vegetation. However, further increases in vegetation density did not enhance hyporheic exchange. Moreover, our results show that the hyporheic exchange velocity scaled with the square root of the sediment permeability. These findings provide theoretical guidance for engineers to estimate the hyporheic exchange rate in a vegetated channel and design effective restoration projects using aquatic vegetation.

S. H. Huang and R. Nuli are co-first authors.

Key Points:

- Index-match experiments and coupled numerical simulations reveal detailed vertical flow paths around vegetation stems
- Stem-scale vertical flow and canopy-scale subsurface flow govern hyporheic exchange, as confirmed by experimental and numerical analyses
- Hyporheic exchange rate increased four times in a vegetated channel compared to a bare channel but did not increase with vegetation density

Supporting Information:

Supporting Information may be found in the online version of this article.

Correspondence to:

J. Q. Yang,
judyyang@umn.edu

Citation:

Huang, S. H., Nuli, R., Kang, P. K., Shen, L., & Yang, J. Q. (2025). Experimental and numerical investigation on the impact of emergent vegetation on the hyporheic exchange. *Water Resources Research*, *61*, e2025WR040217. https://doi.org/10.1029/2025WR040217

Received 12 FEB 2025
Accepted 30 SEP 2025

1. Introduction

Hyporheic exchange is commonly referred to as the exchange of water and chemicals across the sediment-water interface in aquatic environments (Hester & Doyle, 2008; Stonedahl et al., 2010; Tonina & Buffington, 2009). The chemicals include gases (O'Connor & Hondzo, 2008; Tseng & Tinoco, 2022), solutes (Chandler et al., 2016; Marion et al., 2002), and organic matters (Mueller et al., 2021; Schaper et al., 2019). The hyporheic exchange of these chemicals has a great impact on both the biogeochemical cycle (Boano et al., 2010; Li et al., 2017) and the fate of pollutants (Grant et al., 2014; McCallum et al., 2020) in rivers, streams, and other aquatic environments.

In-channel vegetation is an important component of rivers, streams, and many other aquatic ecosystems, yet its role in hyporheic exchange remains poorly understood (Yang, 2024). Vegetation increases flow resistance (Cheng & Nguyen, 2011; Dupuis et al., 2016; D'Ippolito et al., 2019), dissipates mean flow energy (Nepf, 1999; Xu & Nepf, 2020), and produces additional turbulence (Kitsikoudis et al., 2020; Neumeier, 2007). By altering the surface flow, in-channel vegetation has a great impact on sediment transport (Liu & Nepf, 2016; Tseng & Tinoco, 2021; Yang et al., 2016) and pollutant fate (Boano et al., 2014) in aquatic environments. Furthermore, in-channel vegetation is known to induce hyporheic exchange (Huang & Yang, 2022; Jin et al., 2023; Yuan et al., 2021) because the presence of vegetation stems increases the heterogeneity of spatial pressure distribution

at the sediment-water interface (Jin et al., 2023; Nepf & Koch, 1999; Yuan et al., 2021) and generates additional near-bed turbulence (Nepf, 1999, 2012; Tanino & Nepf, 2008). To investigate the impact of vegetation, including both the flourishing biofilms and macrophytes, on the nutrient uptake in a river corridor, previous studies conducted reach-scale solute injections and estimated the uptake velocities by fitting the transport model with breakthrough curves (Aubeneau et al., 2016; Roche et al., 2019). In recent years, the exchange rate between the surface flow and fluid in subsurface region, which is related to the hyporheic exchange, has been considered in the modeling of the breakthrough curves (Drummond et al., 2014; Volponi et al., 2025). However, the parameters of such transport models required site-specific calibrations, which may impede the application of the model in the design of new restoration projects. The fundamental knowledge of vegetation-induced hyporheic processes obtained by controlled laboratory experiments and numerical simulations should provide the insight to estimate the parameters used in transport models.

Among various vegetation types, emergent vegetation, that is, the rigid plant that occupies the whole water column (Nepf, 2012), is widespread in aquatic ecosystems worldwide and known to play a significant role in controlling hydrobiogeochemical processes. For example, emergent vegetation canopy could enhance nitrate (NO_3^-N) removal in riverine sediments (Ullah et al., 2014; Waterman & Hansen, 2024), and increase nutrients removal capacities (Xia et al., 2020). To simplify the complexity of the vegetation morphology, the emergent vegetation is often modeled and studied as a cylinder array (D'Ippolito et al., 2019; Kitsikoudis et al., 2020; Liu et al., 2008). The impact of a cylinder array on surface flow in channels with an impermeable bed has been studied extensively in both laboratory experiments and numerical simulations (Nepf & Koch, 1999; Stoesser et al., 2010; Sumner et al., 2004; Yang et al., 2015). Recent studies also investigated the impact of rigid and cylindrical vegetation stems on the hyporheic exchange through experiments and numerical simulations (Huang & Yang, 2022; Jin et al., 2023; Lv et al., 2022; Tseng & Tinoco, 2022). While laboratory experiments show that emergent vegetation can enhance hyporheic exchange (Huang & Yang, 2022), detailed mechanisms remain poorly understood.

Previous simulations (Jin et al., 2023; Yuan et al., 2021) used a sequential coupling method to model vegetation-induced hyporheic flow. Details of this method are available in Cardenas and Wilson (2007). In these studies, surface flow and pore flow are solved sequentially. The surface flow is solved first, treating the bottom boundary of the fluid domain as a no-silp wall. The resulting pressure field is then imposed as a Dirichlet boundary condition on the top face of the porous media domain. Since only pressure is used to couple the domains—and only the porous domain is influenced by the surface flow, not vice versa—this approach is considered one-way coupling. However, Lv et al. (2022) demonstrated that this unidirectional coupling method may underestimate vegetation-induced hyporheic flux. This is because surface flow structures around vegetation stems can be altered by interactions between surface and pore fluids at the sediment-water interface. A flux boundary condition is typically applied at the sediment-water interface, restricting scalar movement from the porous domain into the surface flow. To better estimate the mass transport in vegetated channels and across the sediment-water interface, it is essential to implement a two-way coupling approach, which simulates both surface and subsurface flows simultaneously. This allows for interaction between the surface flow within the vegetation canopy and the flow in the permeable bed, enabling scalar transport to be treated as continuous throughout the entire simulation domain.

Here, we combine laboratory experiments and coupled numerical simulations to study the hyporheic exchange process within an emergent vegetation canopy in a channel with a permeable bed. We measured the detailed flow field within an emergent vegetation canopy in a channel with a gravel bed using detailed particle image velocimetry (PIV). Additionally, we tracked the migration of fluorescent dye plumes in a channel with an optically accessible sediment bed and quantified the subsurface flow velocity. Fully coupled simulations were conducted to simultaneously model surface and hyporheic flow by solving the Navier-Stokes equations, which describe the balance of inertia, pressure and viscous forces acting on a fluid element. A penalization term was added to these equations to represent the additional drag imposed by the porous sediment, effectively modeling the increased resistance experienced by the fluid. In our integrated approach, numerical simulations were designed to replicate the key physical parameters of the flume experiments, including dowel arrangement, vegetation density, and mean surface flow velocity. We validated the simulated surface flow velocity fields against our PIV measurements. The solute transport results from simulations and experiments were then compared to provide mechanistic insights, and we discuss the quantitative differences that arise from the idealizations of the numerical model. The use of periodic boundary conditions in the streamwise direction is one key aspect in this regard, and it is discussed in detail in Results and Discussions. In this study, we demonstrate how vegetation-induced hyporheic exchange

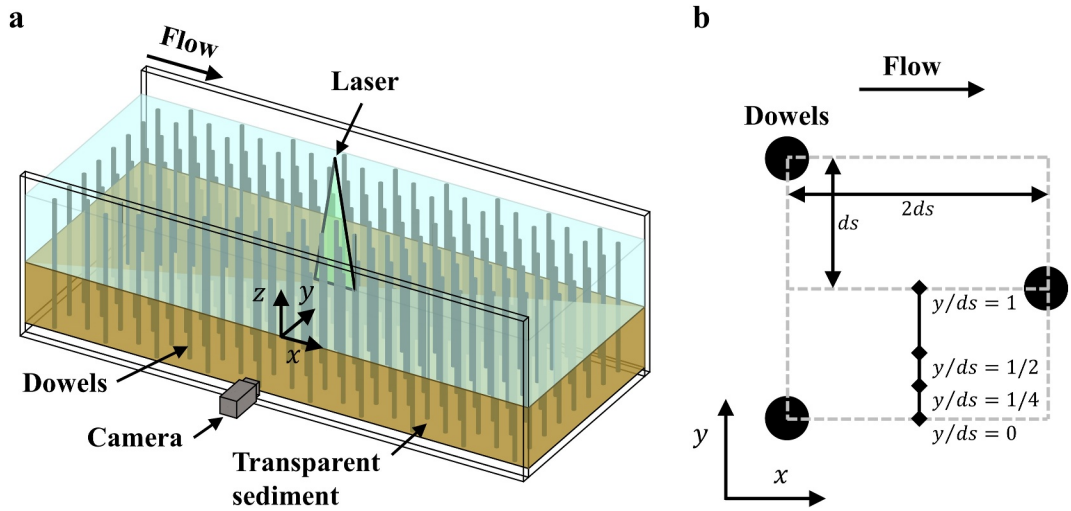

Figure 1. The schematic diagram of the experimental setup. (a) Experimental setup of the channel with emergent vegetation canopy. (b) The horizontal locations where the mean streamwise surface flow velocity profiles were measured. Here, $2ds$ was the lateral center-to-center distance between two dowels.

varies with varying vegetation densities, sediment permeability, and mean streamwise surface flow velocities. Finally, we discuss how our results will facilitate future prediction of vegetation-induced hyporheic exchange in a channel with an emergent vegetation canopy.

2. Materials and Methods

In this study, we combined laboratory flume experiments and coupled numerical simulations to demonstrate how emergent vegetation affect hyporheic exchange. The experimental setup is described in Section 2.1, and the numerical setup is described in Section 2.2.

2.1. Experimental Setup

The experiment was conducted in a horizontal race-track water-recirculating flume at the St. Anthony Falls Laboratory of the University of Minnesota. The length and width of the channel were 14 and 0.6 m, respectively. The water depth was 20 cm. The flow was driven by two thrusters (T200 Thruster; BlueRobotics, California). To observe the hyporheic flow within an emergent vegetation canopy, we used translucent acrylic dowels with a diameter of $d_v = 6.4 \pm 0.1$ mm and a length of 38 cm to simulate rigid and cylindrical vegetation, similar to marsh grasses with stem diameters ranging from 1 to 10 mm (Arenovski & Howes, 1992; Nepf, 2012). The dowels were arranged in a staggered pattern (Figure 1b) in the 1.5 m-long straight test section of the flume (Figure 1a) and were inserted through the whole sediment depth. The lateral center-to-center distance between two dowels was $2ds = 5.0, 2.8$ and 2.6 cm, respectively. The related frontal area per unit vegetation canopy volume, or the spatially averaged area of vegetation dowels normal to the flow, was $a = 2.5, 7.6$ and 9.8 m^{-1}, which overlaps with the typical range of the marsh grasses, $a = 1$ to 7 m^{-1} (Nepf, 2012). The resulting vegetation densities, or the solid volume fraction of the vegetation dowels, were $\phi_v = \frac{\pi}{4} a d_v = 0.012, 0.038,$ and 0.05, respectively. The bottom of the test section was filled with 15-cm-deep transparent spherical hydrogel beads. The hydrogel beads had a diameter of 5.6 ± 0.6 mm, representing gravel sediment (Das, 2021). The corresponding porosity of the sediment was 0.3 (Huang & Yang, 2022, 2023). We estimated the permeability of the sediment made of hydrogel beads using the Karman-Cozeny relationship: $k = \phi_s^3 d_s^2 / 180(1 - \phi_s)^2 = 9.6 \times 10^{-3}$ mm^2 (Voermans et al., 2018), which falls in the range of a clear gravel 1.0×10^{-3} mm$^2 < k < 1.0 \times 10^{-1}$ mm^2 (Das, 2021). The refractive index of the hydrogel beads was similar to water, which provided an optically accessible sediment and allowed us to directly visualize the hyporheic flow motions by tracking the dye within the sediment bed. The dimensions of the experiments and the flow and vegetation configurations were summarized in Table S1 in Supporting Information S1 and Table 1, respectively.

Table 1
The Configurations of the Experiment and Simulation Cases

Tested types	Case no.	Vegetation density (ϕ_v)	Avg. Flow velocity ($\overline{U}$, cm/s)	Porosity (ϕ_s)	Permeability (k, mm^2)	Re_v [a]
Experiments	E-F-01	0	1.7	0.3	9.6×10^{-3}	–
	E-F-02	0	4.1	0.3	9.6×10^{-3}	–
	E-F-03	0	6.7	0.3	9.6×10^{-3}	–
	E-F-04	0	15.6	0.3	9.6×10^{-3}	–
	E-S-01	0.012	1.2	0.3	9.6×10^{-3}	2,962
	E-S-02	0.012	2.5	0.3	9.6×10^{-3}	6,171
	E-S-03	0.012	3.6	0.3	9.6×10^{-3}	8,886
	E-S-04	0.012	4.6	0.3	9.6×10^{-3}	11,355
	E-M1-01	0.038	1.5	0.3	9.6×10^{-3}	1,161
	E-M1-02	0.038	2.0	0.3	9.6×10^{-3}	1,548
	E-M1-03	0.038	2.7	0.3	9.6×10^{-3}	2,090
	E-M1-04	0.038	3.3	0.3	9.6×10^{-3}	2,555
	E-D-01	0.05	0.7	0.3	9.6×10^{-3}	467
	E-D-02	0.05	1.6	0.3	9.6×10^{-3}	1,068
	E-D-03	0.05	2.4	0.3	9.6×10^{-3}	1,602
	E-D-04	0.05	3.6	0.3	9.6×10^{-3}	2,403
Simulations	S-F-01	0	1.6	0.3	9.6×10^{-3}	–
	S-F-02	0	3.6	0.3	9.6×10^{-3}	–
	S-F-03	0	4.5	0.3	9.6×10^{-3}	–
	S-S-01	0.012	1.6	0.3	9.6×10^{-3}	3,949
	S-S-02	0.012	3.6	0.3	9.6×10^{-3}	8,886
	S-S-03	0.012	4.5	0.3	9.6×10^{-3}	11,108
	S-M1-01	0.038	1.6	0.3	9.6×10^{-3}	1,239
	S-M1-02	0.038	3.6	0.3	9.6×10^{-3}	2,787
	S-M1-03	0.038	4.5	0.3	9.6×10^{-3}	3,483
	S-M2-01	0.043	3.6	0.3	9.6×10^{-3}	2,630
	S-M3-01	0.045	3.6	0.3	9.6×10^{-3}	2,553
	S-D-01	0.05	1.6	0.3	9.6×10^{-3}	1,068
	S-D-02	0.05	3.6	0.3	9.6×10^{-3}	2,403
	S-D-03	0.05	4.5	0.3	9.6×10^{-3}	3,004
	S-F-02-P	0	3.6	0.41	4×10^{-2}	–
	S-S-02-P	0.012	3.6	0.41	4×10^{-2}	8,886
	S-M1-02-P	0.038	3.6	0.41	4×10^{-2}	2,787
	S-M2-01-P	0.043	3.6	0.41	4×10^{-2}	2,630
	S-M3-01-P	0.045	3.6	0.41	4×10^{-2}	2,553
	S-D-02-P	0.05	3.6	0.41	4×10^{-2}	2,403

Note. In the case number, for the first letter, "E" represents experiments, and "S" represents simulations; for the second letter, "F" represents flatbed cases, "S" represents sparse vegetation density cases, "M1" represents medium-low vegetation density cases, "M2" represents medium vegetation density cases, "M3" represents medium-high vegetation density cases, and "D" represents dense vegetation density cases, "P" represents cases with high sediment permeability; the numbers indicate the mean streamwise surface flow velocity from low to high. [a]$Re_v = \overline{U} r_v/\nu$. Here $r_v = 8ds^2/3d_v$ is the modified hydraulic radius (Cheng & Nguyen, 2011).

The streamwise and vertical surface flow velocities in the emergent vegetation canopy were measured using two-dimensional PIV. We seeded the water with solid glass beads with a density of $\rho_g = 2{,}600$ kg/m^3 and a mean diameter of $d_g = 35$ μm (3000 E-Spheriglass; Potters Industries Inc., Pennsylvania). The response time of the glass beads to the flow was $\tau_g = d_g^2\rho_g/18\mu = 1.8 \times 10^{-4}$ s (Raffel et al., 2018). The particle Stokes number in the present study was Stk $= \tau_g W_{\max}/l_v \sim 2.8 \times 10^{-4}$, with $W_{\max} \sim 1$ cm/s being the maximum vertical mean

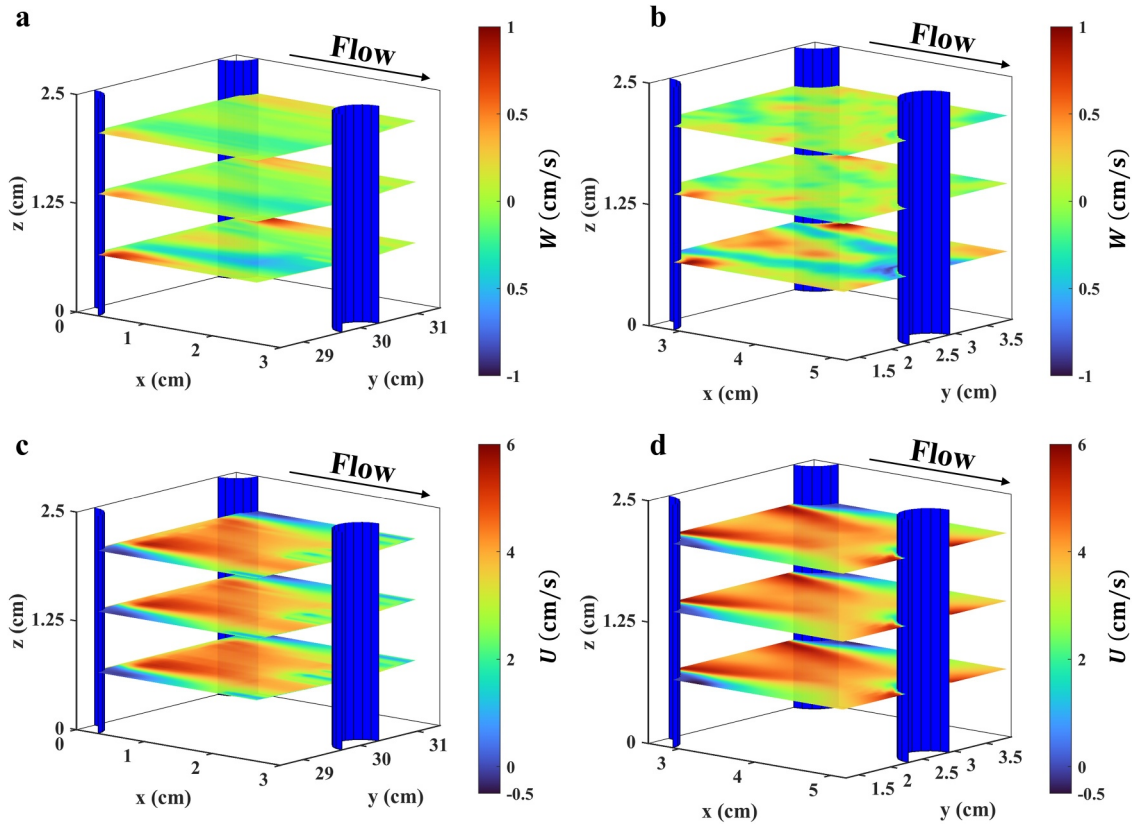

Figure 2. The measured and simulated mean surface flow velocity field of the flow through an emergent vegetation canopy for Case Nos. E-D-04 and S-D-02. One representative pattern of the staggered vegetation is shown here, with the vegetation dowels indicated by the blue quarter and half cylinders. (a) Vertical surface flow velocity measured using particle image velocimetry (PIV). (b) Simulated vertical surface flow velocity. (c) Streamwise surface flow velocity measured using a PIV. (d) Simulated streamwise surface flow velocity. Colors in (a) and (b) indicate the vertical surface flow velocity. Colors in (c) and (d) indicate the streamwise surface flow velocity. The vegetation density was $\phi_v = 0.05$, and the mean streamwise surface flow velocity was $\overline{U} = 3.6$ cm/s. Here, "E" represents experiment cases, "S" represents simulation cases, and "D" represents the dense vegetation density cases.

flow velocity (Figure 2a) and $l_v \sim d_v = 6.4$ mm being the maximum length scale of the eddies in a vegetated channel. The particle Stokes number of the glass beads was smaller than 10^{-1} and should provide an acceptable flow tracing accuracy (Raffel et al., 2018). The seeding particles were illuminated by a 2-mm-thick green laser sheet of 2-W energy at 532 nm from the top of the flume (LSR532F; Lasever, China), and the locations of the particles were imaged by a side-looking camera with a maximum resolution of 1,224 × 1,024 pixels (BFS-U3-51S5M-C; FLIR Systems, Wilsonville). A 5-cm-wide by 12-cm-long by 3-mm-thick 3D-printed perforated board was attached to the top of the dowels to keep the vegetation dowels vertical and from blocking the field of view. A plastic plate was put on the water surface to eliminate the irregular refraction of the laser sheet caused by the water surface fluctuation. The images were taken by the side-looking camera with a frame rate of 200 Hz for 120 s between two rows on the dowels, in which space was optically accessible (Figure S1 in Supporting Information S1). Note that the dowels were not index-matching with the flow. We arranged the locations of the dowels to keep them from obstructing the field of view of the camera. The 2D surface flow velocity fields were calculated from the images using the software PIVLab, developed by Thielicke and Sonntag (2021). Our results show that the time average surface flow velocity at each data point reached a convergent value within 2 min (Figure S2 in Supporting Information S1). The flow measurements were taken at 75 cm downstream of the leading edge of the vegetation canopy (in the middle of the test section). In vegetation canopies with similar vegetation density to our cases, the surface flow developed to a relatively stable condition at 50 cm downstream of the leading edge of the vegetation canopy (Rominger & Nepf, 2011). The development of the flow in the vegetation canopy should not have a great impact on our results.

The time-averaged streamwise surface flow velocities were calculated along multiple vertical profiles at several spanwise locations, specifically at $y/ds = 0, 1/4, 1/2,$ and 1 (Figure 1b). We then calculated the spatially averaged streamwise surface flow velocity $\overline{U}$ by averaging velocity along these four profiles with weights 12.5%, 25.0%, 37.5%, and 25.0% for the measurements at $y/ds = 0, 1/4, 1/2,$ and 1, respectively. The weights of each measurement represent the percentage of length each vertical profiles cover along the spanwise transect (Huang & Yang, 2022; Yang et al., 2015).

To reconstruct the surface flow velocity field, we measured the instantaneous streamwise and vertical surface flow velocities at 32 evenly spaced (1 mm apart) lateral locations between two rows of dowels within a repetitive horizontal plan in the vegetation canopy (Figure S1 in Supporting Information S1). We measured the flow field upstream and downstream of a representative stem located at the center of the channel ($y = 30$ cm) and in the middle of the vegetation canopy ($x = 0$ cm). Afterward, we reconstructed the three-dimensional distributions of the time-averaged streamwise and vertical velocities based on the measured data point using linear interpolation. The vertical flows around the vegetation stems rapidly exchange the nutrient and dissolved inorganic carbon between the pore water and near-bed surface water column, which affects the nutrient intake of the plant via leaves and could thus change the canopy ecology (Nepf & Koch, 1999). To quantify the vertical exchange in the water column at different depths, we calculated the upward and downward vertical flow rate, Q_{up} and Q_{down} [m^3/s]. Q_{up} was obtained by integrating the absolute value of positive (upwelling) flow velocities across the regions where the flow was upward in the selected horizontal plan, while Q_{down} was calculated similarly for the regions with negative (downward) flow velocities. These flow rates were then normalized by the area of the selected horizontal plane to calculate the vertical upward and downward flux q [m/s].

To investigate the impact of the vegetation density on the hyporheic exchange rate, we conducted hyporheic exchange experiments with three vegetation densities including zero, namely $\phi_v = 0.0, 0.012,$ and 0.05 at different mean streamwise surface flow velocities ($\overline{U}$). We conducted the experiments following the procedure of our previous work (Huang & Yang, 2022). We injected the dye uniformly into the top 5 cm of the sediment layer, and the dye concentration in the sediment was detected by a downward-looking camera after the surface flow was started. Our calibration showed that the dye concentration in the transparent sediment has a linear relationship with its fluorescent intensity (Figure S6 in Huang & Yang, 2022). The hyporheic exchange velocity V_H was estimated by fitting the mass transfer equations $\frac{dC_s}{dt} = -V_H \frac{A_{\text{SWI}}\phi_s}{V_{ol,s}}(C_s - C_w)$ and $\frac{dC_w}{dt} = -V_H \frac{A_{\text{SWI}}\phi_s}{V_{ol,w}}(C_w - C_s)$ to the dye concentration versus time curve during $t = 0.3$-2 hours, when the dye decreased spatially uniformly in the vegetation canopy (Huang & Yang, 2022). Here, C_s and C_w are the dye concentrations, A_{SWI} is the area where dye was exchanged [m^2], and $V_{ol,s}$ and $V_{ol,w}$ are the volumes of fluid in the surface and subsurface regions [m^3]. The mass transfer equations were solved numerically and the V_H was chosen to minimize the root mean squared error between the measured and solved dye concentration versus time curves. The period of flow development at the beginning of the experiment was a few minutes, which was relatively short compared to the time scale of the whole experiment (>16.6 hr), and the data within this period was not included in the fitting process of V_H. The details of the fitting process can be found in Huang and Yang (2022). We conducted experiments in a dark room. The background illumination would not change with time. In addition, we ran each exchange experiment for 16.6 hr and only included the data during $t = 0.3$-2 hours in the fitting process of V_H, in which the effect of the photobleaching of the dye was small. The background illumination and photobleaching should not have a great impact on our results. Note that the hyporheic exchange velocity defined here is $V_H = D_e/\delta_D$, where D_e is the effective diffusion coefficient across the sediment-water interface [m^2/s] and δ_D is the mixing layer thickness in the sediment bed [m]. The molecular, dispersive, and turbulence diffusivities in our experiments could be included in V_H and D_e as in previous studies (O'Connor & Harvey, 2008; Voermans et al., 2018).

2.2. Numerical Simulations

2.2.1. Simulation for Surface and Subsurface Flows

To further understand the impact of the emergent vegetation canopy on hyporheic exchange in detail, we simulated surface flow and hyporheic flow simultaneously using modified Navier-Stokes equations. The governing equations for the motion of an incompressible and Newtonian fluid are as follows:

$$\nabla \cdot \boldsymbol{u} = 0, \tag{1a}$$

$$\frac{\partial \boldsymbol{u}}{\partial t} + \boldsymbol{u} \cdot \nabla \boldsymbol{u} = -\frac{1}{\rho}\nabla p + \nu \nabla^2 \boldsymbol{u} + \boldsymbol{g} + \boldsymbol{a}_s. \tag{1b}$$

Here $\boldsymbol{u}$ is the instantaneous fluid velocity [m/s], ρ is the fluid density [kg/m^3], ν is the fluid kinematic viscosity [m^2/s], p is the pressure [Pa], $\boldsymbol{g}$ is the gravitational acceleration [m/s^2], and $\boldsymbol{a}_s$ is the Immersed Boundary forcing [m/s^2] applied to account for the effects of vegetation, which are modeled as rigid bodies within the simulation domain. The determination of this forcing term was described in Cui et al. (2018).

To model flow in the porous bed, we modified the abovementioned Navier-Stokes equations using the penalization method (Bruneau & Mortazavi, 2008; Iliev & Laptev, 2004), which includes penalization terms corresponding to the additional resistance encountered by the flow in the porous bed. We considered both linear Darcy and non-linear Forchheimer equations for the additional flow resistance (Cimolin & Discacciati, 2013). This method provides us with the flexibility to simulate flows in the entire computational domain, including surface water column and porous sediment bed, by solving the same modified Navier-Stokes equations:

$$\rho\left(\frac{\partial \boldsymbol{u}}{\partial t} + (\boldsymbol{u}\cdot\nabla)\boldsymbol{u}\right) - \mu\nabla^2\boldsymbol{u} + \nabla p + \left(\frac{\mu}{k}\boldsymbol{u} + \frac{\rho C_F}{\sqrt{k}}\,|\boldsymbol{u}|\boldsymbol{u}\right)\zeta_p - \rho\boldsymbol{g} - \rho\boldsymbol{a}_s = 0,$$

$$H(\psi,\epsilon) = \begin{cases} 1 & \psi > \epsilon \\ \frac{1}{2}\left[1 + \frac{\psi}{\epsilon} + \frac{1}{\pi}\sin\left(\frac{\psi\pi}{\epsilon}\right)\right] & -\epsilon < \psi < \epsilon \\ 0 & \psi < -\epsilon \end{cases},$$

$$\zeta_p = H\left(z_p^* - z^*, 2\cdot\Delta z\right), \text{where } z_p^* = 1 \tag{2}$$

The first term in Equation 2 represents the unsteady and convective effects, the second term accounts for the viscous effects, and the third term represents the pressure gradient effects. The fourth term represents the porous media modeling term, with the mask, ζ_p, ensuring the resistance terms are only applied in the porous zone. The transition of the penalization term at the sediment-water interface is smoothed. This is accomplished by defining the mask function, ζ_p, using a smoothed Heavyside function, $H(\psi,\epsilon)$, which creates a gradual transition between the porous and fluid domains. The smoothed Heavyside function, which transitions from 0 to 1 over a distance of 2ϵ is defined in Equation 2. The mask ζ_p is then constructed at the interface plane, defined by $z^* = z_p^*$, by setting $\psi = z_p^* - z^*$ and using smoothing parameter $\epsilon = 2\Delta z$.

The porous medium is characterized by sediment permeability k [m^2] and the inertial resistance coefficient C_F. Flow velocity $\boldsymbol{u}$ describes the actual velocity in the fluid zone and seepage velocity in the porous zone. Changing the governing equation into a non-dimensional form leads to two additional non-dimensional numbers corresponding to the viscous and inertial resistance, respectively.

$$\frac{\partial \boldsymbol{u}^*}{\partial t} + \boldsymbol{u}^*\cdot\nabla\boldsymbol{u}^* + \nabla p^* - \frac{1}{Re}\nabla^2\boldsymbol{u}^* - \frac{1}{Fr^2}\boldsymbol{g} - \boldsymbol{a}_s^* + Gr_\nu\boldsymbol{u}^* + Gr_i|\boldsymbol{u}^*|\boldsymbol{u}^* = 0 \tag{3}$$

Here, the non-dimensional numbers are $Gr_\nu = \frac{\mu L}{\rho\overline{U}k}, Gr_i = \frac{\rho L C_F}{\rho\sqrt{k}}, Re = \frac{\rho\overline{U}L}{\mu}$, and $Fr = \frac{\overline{U}}{\sqrt{gL}}$. In the current implementation, we used a second-order finite-difference method for spatial discretization and a second-order Runge-Kutta (RK2) method for time marching. The fractional step method (He, 2022; Kim & Moin, 1985) was applied to preserve the divergence-free nature of the velocity field.

2.2.2. Scalar Transport Modeling

To quantify the hyporheic exchange, we simulated scalar transport using a decoupled method. This approach treats the solute as a passive tracer, assuming its presence has a negligible effect on fluid properties and thus provides no feedback on the flow field itself. This assumption is valid for the low-concentration fluorescent dye used in this study but would not be suitable for scenarios involving reactive transport. The transport of the passive scalar is governed by the following equation:

$$\frac{\partial C}{\partial t}+\left(\boldsymbol{u}\cdot\frac{\partial C}{\partial x}+v\cdot\frac{\partial C}{\partial y}+w\cdot\frac{\partial C}{\partial z}\right)=D_x\frac{\partial^2 C}{\partial x^2}+D_y\frac{\partial^2 C}{\partial y^2}+D_z\frac{\partial^2 C}{\partial z^2} \tag{4}$$

Here, C is the tracer concentration, $(\boldsymbol{u},v,w)$ are instantaneous flow velocities, and (D_x,D_y,D_z) are the effective diffusion coefficients. The fluid zone is in the diffusion regime, characterized by isotropic dispersion. In the porous bed, the dispersion is anisotropic, namely

$$\text{Fluid zone}: D_x=D_y=D_z=D_m \tag{5a}$$

$$\text{Porous zone}: D_x=D_L;\ D_y=D_z=D_T \tag{5b}$$

To estimate the effective diffusion coefficients in the porous bed, we dynamically calculated the effective longitudinal and transverse dispersion coefficients using the functions f_L and f_T, which are dependent on the regime, as detailed in Delgado (2007) for a randomly packed bed.

$$D_L=D'_m\cdot f_L\left(Pe'^E_m,Sc\right), \tag{6a}$$

$$D_T=D'_m\cdot f_T\left(Pe'^E_m,Sc\right). \tag{6b}$$

Here, $D'_m=D_m/\tau_d$ is the effective molecular diffusivity (Ghanbarian et al., 2013) with D_m representing the molecular diffusivity and $\tau_d=(L_d/L_s)^2$ presenting the diffusive tortuosity defined by the path traveled by fluid particles in the porous medium. L_d is the distance traveled by the fluid particles in the porous medium, and L_s is the straight-line distance it would have traveled if there were no obstructions (Ghanbarian et al., 2013). The value of τ_d was obtained using a relation from Lanfrey et al. (2010) for fixed beds with randomly packed identical particles, which provides a relation between the porosity and tortuosity. We calculated the Eulerian Peclet number $Pe^E_m=\left(\boldsymbol{u}_s/\phi_s\right)d_p/D'_m$ and the effective Eulerian Peclet number $Pe'^E_m=\left(\boldsymbol{u}/\phi_s\right)d_p/D'_m$ following Nguyen and Papavassiliou (2020). Here, $\boldsymbol{u}_s$ is the seepage velocity, ϕ_s is sediment porosity, and d_p is the particle diameter. The term $\boldsymbol{u}_s/\phi_s$ is the pore velocity. $Sc=\mu/\rho D_m$ is Schmidt number.

Equation 4 can be converted into a non-dimensional form:

$$\frac{\partial C^*}{\partial t^*}+\left(\boldsymbol{u}^*\cdot\frac{\partial C^*}{\partial x^*}+v^*\cdot\frac{\partial C^*}{\partial y^*}+w^*\cdot\frac{\partial C^*}{\partial z^*}\right)=\frac{1}{ReSc_x}\frac{\partial^2 C^*}{\partial x^{*2}}+\frac{1}{ReSc_y}\frac{\partial^2 C^*}{\partial y^{*2}}+\frac{1}{ReSc_z}\frac{\partial^2 C^*}{\partial z^{*2}} \tag{7}$$

Here, $Sc_x=\frac{\mu}{\rho\cdot D_x}$, $Sc_y=\frac{\mu}{\rho\cdot D_y}$, and $Sc_z=\frac{\mu}{\rho\cdot D_z}$.

2.2.3. Simulation Setup

To numerically model the large-scale vegetation canopy of the flume experiment, we simulated the flow in a computationally efficient, representative section of the dowel array (see Figure S3 in Supporting Information S1 for a schematic). By applying periodic boundary conditions in the streamwise and spanwise directions, this domain simulates the behavior of an infinite vegetation canopy. To ensure a direct link between the experiments and simulations in this study, key physical parameters from the experiment were replicated in the simulation, including the dowel diameter, the staggered dowel arrangement, sediment porosity, and the mean streamwise surface flow velocity. Specifically, the dowels were arranged in a staggered pattern with a center-to-center distance of $2ds$ (Figure 1b). We simulated flow in vegetated channels with different vegetation densities with varying ds. The dimensions of the simulation domain in the x and y directions were $8ds$ and $4ds$, respectively, while the dimension of the simulation domain in the vertical direction remained the same in all the simulations ($z=-10$ to 10 cm). We used the periodic boundary condition in the streamwise and spanwise directions. In the vertical direction, we applied free-slip and no-slip boundary conditions at the top and bottom boundaries, respectively. The flow was driven by a pressure gradient in the streamwise direction. To maintain a constant averaged streamwise surface flow velocity $\boldsymbol{u}_c$, we tuned this pressure gradient according to the following equation:

$$\frac{dp}{dx}(t) = K_p \Delta \boldsymbol{u}_b(t) + K_I \int \Delta \boldsymbol{u}_b(t)\, dt \tag{8}$$

Here $\Delta \boldsymbol{u}_b(t) = \boldsymbol{u}_c - \overline{U}(t)$, where $\overline{U}(t)$ is the averaged streamwise surface flow velocity at instant t. We performed preliminary tests to select the proportional (K_p) and integral (K_I) gains, setting them to 30 and 7.5, respectively, for all simulations presented in this study. These gains were chosen to ensure rapid convergence to the target velocity, $\boldsymbol{u}_c$, while minimizing overshoot and steady-state error. A detailed visualization of the controller's performance for a representative case is provided in Figure S4 in Supporting Information S1, which shows the evolution of the mean streamwise velocity, $\overline{U}$, the controller effort (pressure gradient) and the accuracy of the controller. The controller achieved the target velocity with a steady-state error of less than 0.5% and did not introduce any noticeable numerical instability into the simulation. Other convergence parameters are provided in Table S2 in Supporting Information S1.

At the beginning of each simulation, the flow field was initialized with zero velocity everywhere in the simulation domain. By imposing a streamwise pressure gradient, the flow velocity approached $\boldsymbol{u}_c$. Once the flow field became fully developed, we initialized scalar transport modeling by setting the scalar concentration $C = 1$ in the top 5 cm of the sediment layer and $C = 0$ everywhere else. In total, 20 simulations were conducted to systematically investigate how vegetation-induced hyporheic exchange varies with different physical conditions. We varied three key parameters: vegetation density (ϕ_v), sediment permeability (k) and mean streamwise surface flow velocity ($\overline{U}$). The general simulation parameters are summarized in Table S3 in Supporting Information S1, while Table 1 details the specific configurations for each of the 20 cases, which systematically vary these three key parameters. The vegetation Reynolds numbers $Re_v = \overline{U} r_v / \nu$ in our experiments and simulations ranged from 467 to 11355 (Table 1), which cover a wide range of the flow conditions. Here, r_v is the modified hydraulic radius calculated by the ratio between the volume of the water column and vegetation effective wetted area (Cheng & Nguyen, 2011).

2.2.4. Grid Sensitivity Analysis

A grid sensitivity analysis was performed to ensure the numerical results were independent of the mesh resolution. The analysis was conducted for dense vegetation density and medium flow velocity case (Case No. S-D-02 in Table 1) with mean streamwise flow velocity $(\overline{U})$ of 3.6 cm/s, vegetation solid fraction (ϕ_v) of 0.05 and porosity (ϕ_s) of 0.3. Three different grid resolutions were tested:

- Coarse Mesh: 144 × 72 × 240 (2.5 million cells)
- Baseline Mesh: 160 × 80 × 320 (4.1 million cells)
- Fine Mesh: 176 × 88 × 400 (6.2 million cells)

The baseline mesh was used in our primary simulations. The fine mesh was constructed with a 10% refinement in the streamwise and spanwise directions and a 25% refinement in the vertical direction to better resolve the sediment-water interface. We compared the key outputs, including scalar washout curves from the porous zone and the calculated hyporheic exchange velocity, V_H. The washout curves from the baseline and the fine meshes were nearly identical (Figure S5 in Supporting Information S1), indicating the overall transport dynamics were well-captured by the baseline grid. The evolution of V_H plot also shows no significant difference between the baseline and the fine grid setting (Figure S6 in Supporting Information S1). Furthermore, the final converged V_H value for the fine mesh was within 1% of the value from the baseline mesh (Table S4 in Supporting Information S1). Given the significant additional computational cost of the fine mesh, the baseline mesh was deemed sufficient for this study.

2.2.5. Turbulence Resolution

We checked the quality of the mesh by computing the ratio of the local grid size (Δ) to the Kolmogorov length scale (η). The grid size was calculated as $\Delta = (\Delta x \cdot \Delta y \cdot \Delta z)^{1/3}$, and the Kolmogorov scale was calculated as $\eta = \left(\frac{\nu^3}{\varepsilon}\right)^{1/4}$. Here the ν is the kinematic viscosity and ε is the turbulent dissipation rate, computed directly from the fluctuating strain-rate tensor, $s_{i,j}'$ as $\varepsilon = 2\nu\langle s_{i,j}' s_{i,j}' \rangle$. As shown in the contour plots in Figure S7 in Supporting

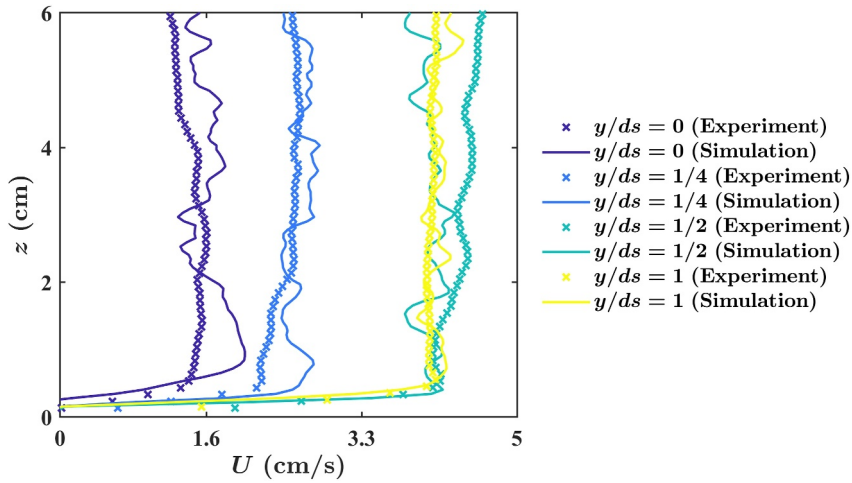

Figure 3. The measured and simulated time-averaged streamwise surface flow velocity profiles at $y/ds = 0, 1/4, 1/2, 1$ for Case Nos. E-D-04 and S-D-02 in Table 1. The spanwise locations of the surface velocity profiles are shown in Figure 1b. The presented data points were extracted at a single x coordinate in the middle of two rows of the stems. The color indicates the locations of the velocity profiles. The vegetation density was $\phi_v = 0.05$, and the mean streamwise surface flow velocity was $\overline{U} = 3.6$ cm/s. Here, "E" represents experiment cases, "S" represents simulation cases, and "D" represents the dense vegetation density cases.

Information S1, the resulting ratio of Δ/η is below 2.5 for the entire domain. Following the recommendations of Yeung and Pope (1989) and the procedure in Bilbao-Ludena and Papadakis (2023), we consider this grid resolution sufficient to justify the DNS approach without an explicit turbulence model.

3. Results and Discussions

3.1. Impact of Emergent Vegetation Canopy on Surface Flow

To investigate the impact of vegetation on surface flow, we conducted surface flow velocity measurements in the flume by experimentally collecting detailed PIV measurements and by conducting the fully coupled numerical simulations using the penalization model. Here, we used the case with vegetation solid fraction (ϕ_v) of 0.05 and a mean streamwise flow velocity ($\overline{U}$) of 3.6 cm/s (Case No. E-D-04 in Table 1) as our primary scenario, because it had the highest vegetation solid fraction and the maximum mean streamwise surface flow velocity our flume could achieve. Figure 2 compares the measured vertical and streamwise surface flow velocities (Case No. E-D-04) with the simulated velocities (Case No. S-D-02). The simulated spanwise surface flow velocity field is shown in Figure S8 in Supporting Information S1. As shown in Figure 2, the simulated surface flow velocity and the measured surface flow velocity exhibit similar distributions. Upward surface velocity was observed downstream of the dowels, while downward surface flow velocity was observed upstream of the dowels. These stem-scale vertical flow paths were induced by the pressure gradient in the vertical direction as the flow slows down upstream of the dowels, as discussed in previous studies (Lv et al., 2022; Nepf & Koch, 1999; Yuan et al., 2021). Our flow measurements provided more detailed information on the velocity distribution of these vertical flow paths. Our measurements, as described below, demonstrated the magnitude and region of the stem-scale upwelling and downwelling flows around each vegetation dowel. The region of upwelling flow extended 1 to 2 dowel diameters downstream of each dowel, with a maximum velocity of 20% of the streamwise velocity. In contrast, the region of downwelling flow extended 0.5 to 1 dowel diameter upstream of each dowel, with a maximum velocity of 15% of the streamwise velocity.

To further compare the measured and simulated flow fields, we plotted the vertical profile of temporally averaged streamwise surface flow velocity at four representative spanwise locations and at the middle of two rows of the dowels in the stremwise direction (see Figure 1b). As shown in Figure 3, the simulation successfully predicted the vertical distribution of the streamwise surface flow velocity at these representative locations, validating the accuracy of the simulation. The presented data points were extracted at a single x coordinate in the middle of two rows of the stems. The simulation was run until the flow reached a statistically stationary state, as confirmed by

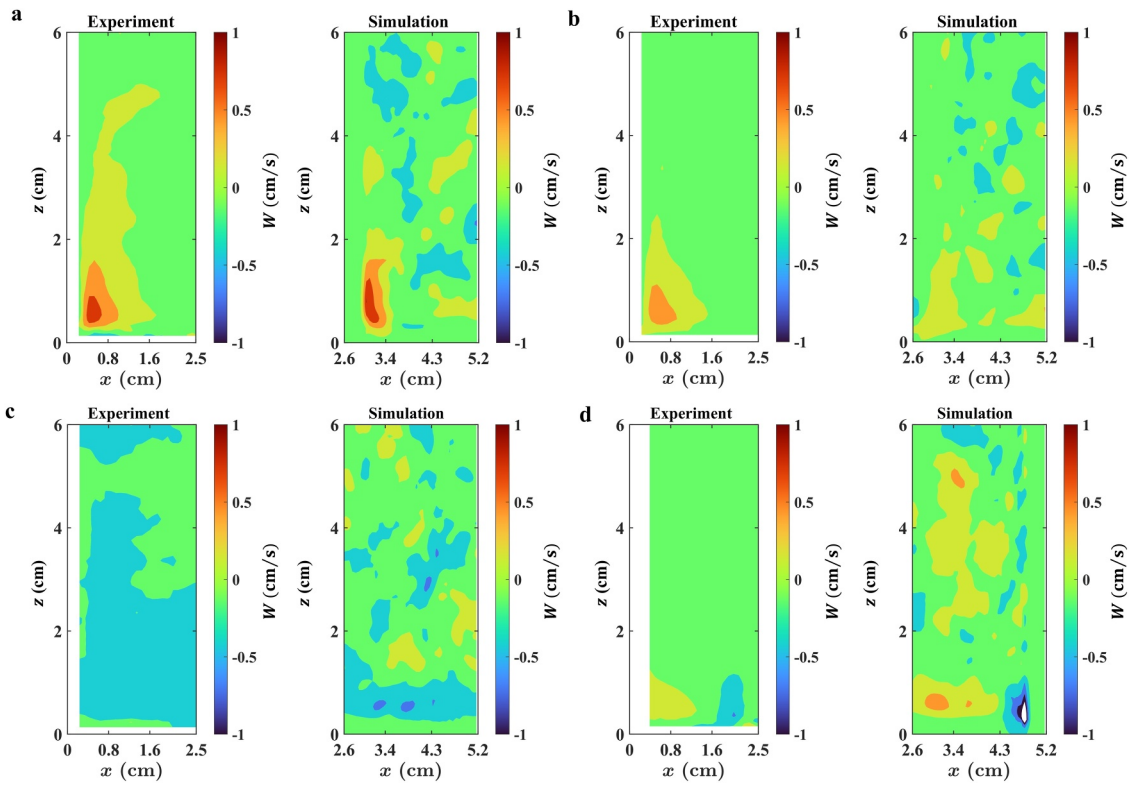

Figure 4. The measured and simulated vertical surface flow velocity fields in x-z plane at various spanwise locations (y-axis) for Case Nos. E-D-04 and S-D-02. (a) Mean vertical surface flow velocity field at $y/ds = 0$. (b) Mean vertical surface flow velocity field at $y/ds = 1/4$. (c) Mean vertical surface flow velocity field at $y/ds = 1/2$. (d) Mean vertical surface flow velocity field at $y/ds = 1$. The vegetation density was $\phi_v = 0.05$, and the mean streamwise surface flow velocity was $\overline{U} = 3.6$ cm/s. Here, "E" represents experiment cases, "S" represents simulation cases, and "D" represents the dense vegetation density cases.

the convergence of Reynolds stresses over time (see Figure S9 in Supporting Information S1 for details). The minor jaggedness observed in the simulated velocity profiles in Figure 3 is likely due to the periodic domain's finite size, which can restrict the largest turbulent length scales thereby influencing the time-averaged flow profiles. The total mean squared errors for four profiles were MSE $= 0.14$ cm^2/s^2 at the points between $z = 0$ and $z = 10$ cm. The largest difference between the experimental and simulation results occurred at the velocity profile on the downstream side of the dowel ($y/ds = 0$ in Figure 1b) and the regions below $z = 1$ cm.

In addition, we compared the measured and simulated vertical velocity fields in the x-y planes at different spanwise locations (Figure 1b) in Figure 4. Stem-scale upwelling and downwelling flows were present in both the measured and simulated temporally averaged vertical velocity fields. Figures 2 and 4 show that the region of upwelling flow on the downstream side of the dowel extended 1.4, 0.6, and 2.0 cm in x, y, and z directions, respectively. On the other hand, the region of downwelling flow on the upstream side of the dowel extended only 0.5, 0.6, and 1.0 cm in x, y, and z directions, respectively, which was smaller than the region of upwelling flow.

We also calculated the measured turbulent kinetic energy (TKE) for the medium-low vegetation density and high flow velocity case with $\phi_v = 0.038$ and $\overline{U} = 3.3$ cm/s (Case No. E-M1-04 in Table 1) to show the field of TKE around the dowels in Figure S10 in Supporting Information S1. The TKE was higher on the downstream side of the dowels, and the spanwise distribution of the TKE was relatively uniform along the z-axis. Note that we calculated TKE using $\text{TKE} = \frac{1}{2}\left(2\overline{u'^2} + \overline{w'^2}\right)$ following Yang et al. (2016), which may underestimate the TKE contributed by lateral components.

Furthermore, to investigate the impact of stem-scale vertical flows on the vertical exchange across the water column, we calculated the measured upward and downward vertical flux of surface flow based on measured mean flow velocity fields, q, at varying vertical locations for the medium-low vegetation density cases with a vegetation density of $\phi_v = 0.038$ and $\overline{U} = 3.3$ cm/s (Case No. E-M1-04). As shown in Figure 5a, the upward and downward

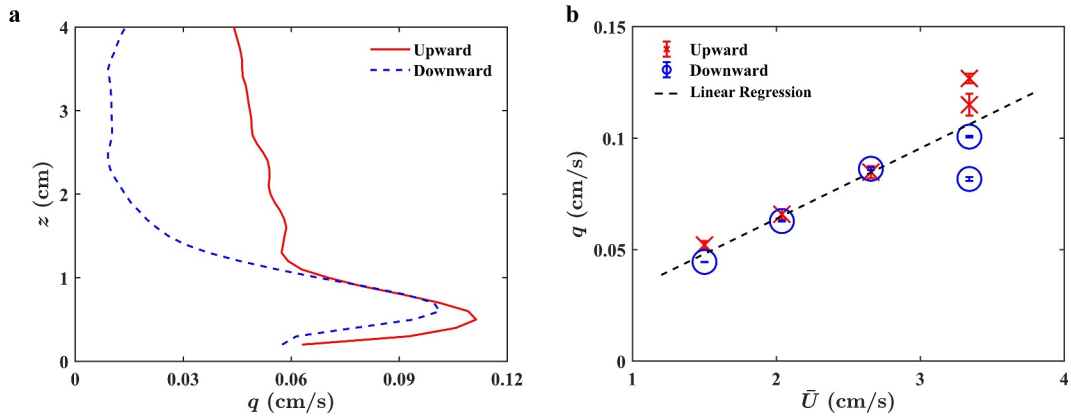

Figure 5. The measured vertical flux q of surface flow within an emergent vegetation canopy with $\phi_v = 0.038$ (Case Nos. E-M1-01 to E-M1-04). The red and blue colors indicate the upward and downward vertical fluxes, respectively. (a) The vertical distribution of the upward and downward vertical flux q for the case with $\overline{U} = 3.3$ cm/s (Case No. E-M1-04). (b) q at $z = 0.6$ cm at various mean streamwise flow velocity $\overline{U}$ (Case Nos. E-M1-01 to E-M1-04). The black dashed line ($y = (31.6x + 0.7) \times 10^{-3}$) represents the linear regression line of q on $\overline{U}$ with $R^2 = 0.82$. Here, "E" represents experiment cases and "M1" represents the medium-low vegetation density cases.

vertical flux q first increased with increasing distance from the bed ($z = 0$ cm), reached its maximum value ($q = 0.11$ cm/s) at $z = 0.6$ cm, and then decreased with further increasing distance from the bed. Meanwhile, our simulations for the dense vegetation density and medium flow velocity cases with $\phi_v = 0.05$ and $\overline{U} = 3.6$ cm/s (Case No. S-D-02) show the same trend (Figure S11a in Supporting Information S1). In addition, we measured the surface flow fields at different streamwise flow velocities $\overline{U}$ for vegetation density $\phi_v = 0.038$ in experiments (Case Nos. E-M1-01 to E-M1-04 in Table 1), which velocities overlap with the range of velocities in the related simulation cases (Case Nos. S-M1-01 to S-M1-03 in Table 1). For the four flow velocities considered here ($\overline{U} = 1.5, 2.0, 2.7$, and 3.3 cm/s), we observed that the maximum q occurred at $z = 0.6 \pm 0.1$ cm, which is about one dowel diameter $d_v = 0.64$ cm, suggesting that the maximum vertical flux occurs at one diameter above the bed in channels with emergent vegetation. Finally, simulation results for the dense vegetation cases with the vegetation density $\phi_v = 0.05$ (Case No. S-D-01 to S-D-03) showed that the locations where maximum q occurred decreased with increasing $\overline{U}$ (Figure S11b in Supporting Information S1).

To estimate the vegetation-induced maximum vertical flux, we plotted the experimentally measured vertical flux q at $z = 0.6$ cm as a function of the mean streamwise flow velocity $\overline{U}$ in Figure 5b for the medium-low vegetation density cases (Case No. E-M1-01 to E-M1-04). We defined the flux q as the spatially averaged upward or downward mean flow velocity across a certain elevation within a repetitive unit of a vegetation canopy (see Methods for details). As shown in Figure 5b, q at $z = 0.6$ cm increased linearly with increasing $\overline{U}$, suggesting that the vegetation-generated near-bed flux increased linearly with increasing mean streamwise surface flow velocity. Note that the data points for the highest velocity cases (Case No. E-M1-04) in Figure 5b included measurements from two separate tests. The highest cross mark and the lowest open circle for the cases with $\overline{U} = 3.3$ cm/s belong to the first test. The cross mark and open circle in the middle for the cases with $\overline{U} = 3.3$ cm/s belong to the second test. It shows an uncertainty of the measurements for high flow velocity cases, which may also cause the difference between upward and downward fluxes above $z = 1$ cm in Figure 5a.

Simulation results for dense vegetation density cases with vegetation density $\phi_v = 0.05$ also showed that q_{max} increased linearly with increasing $\overline{U}$ (Figure S12a in Supporting Information S1, Case No. S-D-01 to S-D-03). Furthermore, vertical flux across the sediment-water interface ($z = 0$ cm) q_{SWI} increased linearly with the maximum vertical flux q_{max} around each stem (Figure S12b in Supporting Information S1), suggesting that the stem-scale flows drive hyporheic exchange.

Finally, our simulation showed that at the same $\overline{U}$, the maximum upward vertical flux $q_{up,max}$ did not increase with increasing vegetation density ϕ_v (Figure S13a in Supporting Information S1). Furthermore, the peak upward vertical velocity on the downstream side of the dowel W_{max} decreased with increasing ϕ_v (Figure S13b in

Supporting Information S1). This result is consistent with a previous study which suggested that the magnitude of the upwelling flow velocity decreased with increasing vegetation density at the same mean flow velocity (Nepf & Koch, 1999). Specifically, at the same $\overline{U}$, increasing ϕ_v increased turbulence mixing, which made the streamwise flow more uniform and reduced the mean streamwise flow velocity gradient, leading to a smaller $W_{\max}$.

These results suggest that the region of upwelling flow around each vegetation stem, extending around 2 to 3 diameters, is larger than the region of downwelling flow, which extends about 1–2 diameters. We also found that the maximum vertical flux $q_{\text{up,max}}$ occurred at $z = d_v$. In addition, $q_{\text{up,max}}$ was independent of the vegetation density under the tested flow conditions. These findings pave the way for predicting the region most impacted by hyporheic exchange around emergent vegetation and other cylindrical structures, such as bridge piers, and for optimizing the design of restoration projects using vegetation.

3.2. The Impact of Vegetation on Subsurface Flow and Hyporheic Exchange

To quantify the impact of vegetation on hyporheic flow, we measured the subsurface flow by tracing the trajectories of a fluorescent dye within the transparent sediment in the flume and simulated the concentration field in the subsurface using an advection-diffusion/dispersion equation (see Methods for details). In both experiments and simulations, we observed a continuous horizontal downstream migration of the dye in the sediments across the vegetation canopy and stem-scale vertical fluxes across the sediment interface driven by the vertical flows discussed in Section 3.1. The canopy-scale dye migration, coupled with the stem-scale vertical fluxes, controlled the total hyporheic exchange. In the following section, we demonstrate the hyporheic exchange in different temporal and spatial scales through two types of dye visualization experiments and scalar transport modeling.

We conducted dye injection experiments with two different injection conditions. First, we injected a small volume of dye (0.2 mL) into the sediment bed at 2.5 cm below the sediment-water interface within the vegetation canopy (green area in Figure 6a) and observed that the dye plume migrated and elongated across multiple dowels in the streamwise direction (Figure 6). The pulse injection allows to better quantify plume spreading. For the dense vegetation density and high flow velocity case with vegetation density $\phi_v = 0.05$ and streamwise velocity $\overline{U} = 3.6$ cm/s (Case No. E-D-04), the average migration velocity of the centroid of the dye plume across multiple stems was 0.033 ± 0.008 cm/s. Our results demonstrate that the dye's horizontal migration occurred continuously in the streamwise direction over the whole canopy. Furthermore, when the dye plume encountered a vegetation dowel, a portion of the dye started being released on the downstream side of the dowel (Figures 6 and 7a). The same process was also observed in our simulation results (Figure 7b).

To demonstrate the hyporheic exchange around each individual dowel in the experiments, we continuously injected the fluorescent dye into the sediment at 2.5 cm below the sediment-water interface and 1 cm upstream of a representative dowel, located in the middle of the vegetation canopy ($y = 30$ cm and $x = 0$ cm). For the medium-low vegetation density and high flow velocity case with vegetation density $\phi_v = 0.038$ and streamwise velocity $\overline{U} = 3.3$ cm/s (Case No. E-M1-04), the injected dye was observed to move downstream within the sediment. After it passed the dowel, it moved upward, exiting the sediment on the downstream side of the dowel, as shown in Figure 7a. The exiting region of the dye on the downstream side of the dowel is the region where the stem-scale upwelling flow was observed (Figure 7a), suggesting that the stem-scale vertical flow drives the stem-scale hyporheic flux. The simulation result is consistent with our experimental observations (Figure 7b).

Furthermore, we compared the overall hyporheic exchange rate measured in the experiment with that estimated from the simulation. At the beginning of the experiment and simulation, the dye was uniformly distributed in the top 5 cm of the sediment layer. Figure S14 in Supporting Information S1 compares the measured and simulated dye concentration versus time curves (washout curves) for the sparse and dense vegetation density and high flow velocity cases with vegetation density ϕ_v of 0.012 and 0.05 at $\overline{U} = 3.6$ cm/s (Case Nos. E-S-03, E-D-04, S-S-02, and S-D-02). Both experiments and simulations show exponential decay in the dye concentration within the sediments in the first 5 min of the test. The decrease in the dye concentration in the sediment was slower in the simulation compared to the experiment, which may be attributed to the periodic boundary condition used in the simulation. This boundary condition allows the dye exiting the downstream boundary of the simulation domain to reenter the upstream boundary, resulting in a smaller decrease in dye concentration compared with the experiments where no additional dye is introduced upstream.

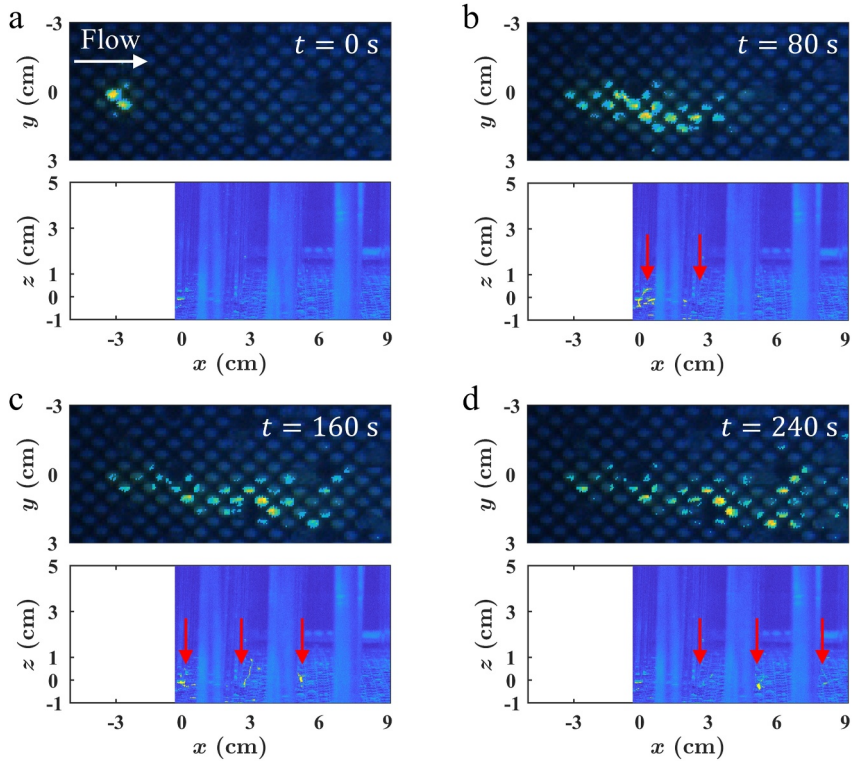

Figure 6. The elongation and migration of a green fluorescent dye plume in the sediment and the release of the dye on the downstream side of the dowels at (a) $t = 0$ s; (b) $t = 80$ s; (c) $t = 160$ s; and (d) $t = 240$ s in Case No. E-D-04, respectively. The upper subplot shows the top view of the channel. The lower subplot shows the lateral view of the channel. The red arrows indicate the locations where the dye moved upward and exited the sediment. The vegetation density was $\phi_v = 0.05$, and the mean streamwise surface flow velocity was $\overline{U} = 3.6$ cm/s. Here, "E" represents experiment cases and "D" represents the dense vegetation density cases.

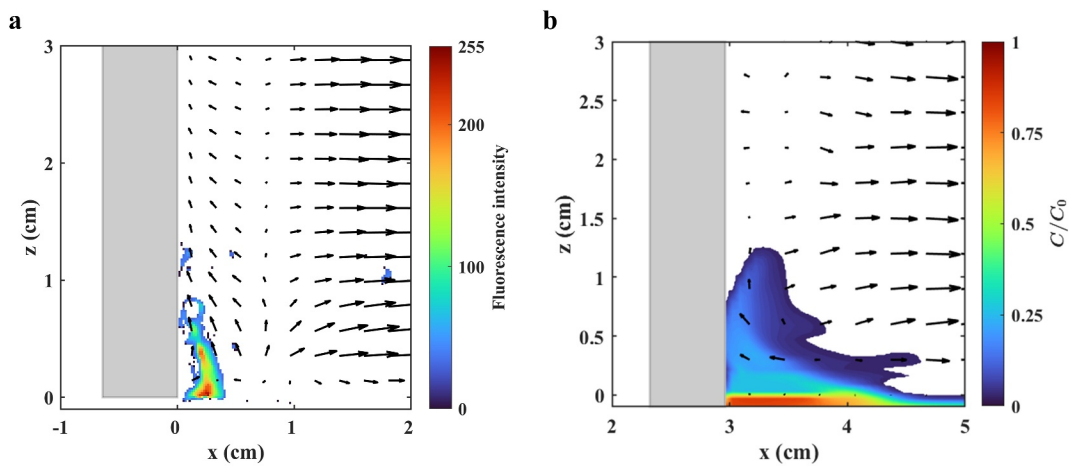

Figure 7. Dye released from the downstream side of a vegetation dowel indicated by the gray square. (a) Results from the dye-visualization experiment in a vegetation canopy with $\phi_v = 0.038$ at streamwise velocity $\overline{U} = 3.3$ cm/s (Case No. E-M1-04). The color indicates the fluorescence intensity of dye released from the sediment bed. The vectors indicate the mean surface flow velocity field measured using a 2D particle image velocimetry. The sediment bed was at $z = 0$ cm. (b) Results from the simulation in a vegetation canopy with $\phi_v = 0.05$ at streamwise velocity $\overline{U} = 3.6$ cm/s (Case No. S-D-02). The color indicates the dye concentration normalized by the initial dye concentration C_0. The vectors indicate the simulated mean surface flow velocity field. Here, "E" represents experiment cases, "S" represents simulation cases, "M1" represents medium-low vegetation density cases, and "D" represents the dense vegetation density cases.

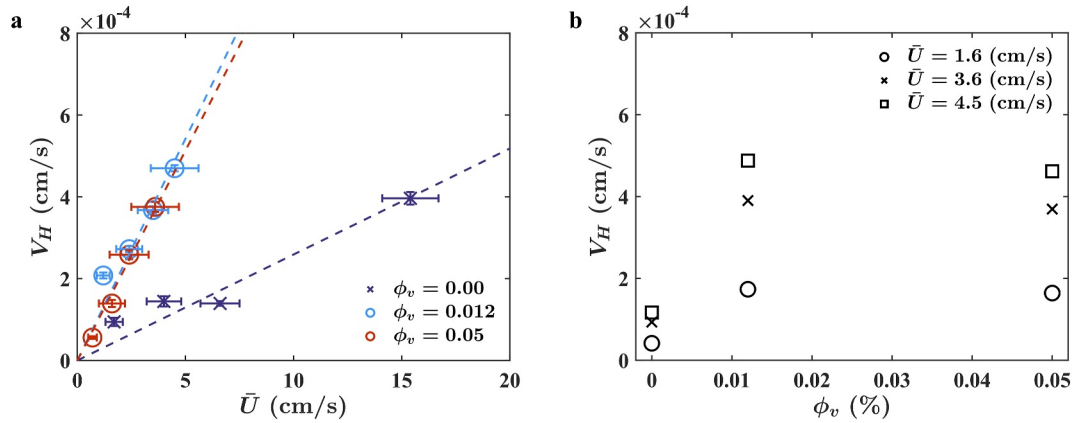

Figure 8. The measured hyporheic exchange velocity V_H at different mean streamwise surface flow velocities $\overline{U}$ for cases with varying vegetation densities $\phi_v = 0$, 0.012, and 0.05. (a) V_H is plotted against surface flow velocity. The crossmarks indicate cases without vegetation. The open circles indicate cases with vegetation. Color represents vegetation density ϕ_v. The dashed lines represent the linear regression lines of V_H on $\overline{U}$. The slopes for cases with $\phi_v = 0.0, 0.012,$ and 0.05 were 0.26×10^{-4}, 1.08×10^{-4}, and 1.03×10^{-4}, respectively. (b) The regression V_H of different ϕ_v at $\overline{U} = 1.6, 3.6,$ and 4.5 cm/s, respectively.

These experiments and numerical simulations suggest that the vegetation-induced hyporheic exchange results from the combined effects of stem-scale vertical flows and canopy-scale horizontal migration. To develop an accurate model to predict the total vegetation-induced hyporheic exchange may require accounting for the interactions of the two processes presented here.

3.3. Impact of Vegetation Density on the Hyporheic Exchange

To investigate the impact of the vegetation density on the hyporheic exchange rate, we conducted hyporheic exchange experiments (see Methods for details). The measured hyporheic exchange velocity is shown in Figure 8a. At the same mean surface flow velocity $\overline{U}$, the V_H was 4 times higher for the cases with vegetation than without (calculated based on the slopes of fitting lines in Figure 8a). However, the hyporheic exchange velocity measured in the sparse vegetation density cases with $\phi_v = 0.012$ (Case Nos. E-S-01 to E-S-04) was similar to the dense vegetation density cases with $\phi_v = 0.05$ (Case Nos. E-D-01 to E-D-04; Figure 8b), suggesting that increasing vegetation density does not increase hyporheic exchange velocity. Note that the V_H fitted here was based on the data when t = 0.3-2 hours; the V_H fitted based on the data in the first 15 min was much higher (Figure S15a in Supporting Information S1).

Using the coupled numerical simulation, we simulated the hyporheic exchange process in a channel with different vegetation densities and different mean streamwise surface flow velocities. For each case, we calculated $V_H = -\frac{dC_s}{dt}\frac{V_{ol,s}}{(C_s - C_w)A_{SWI}\phi_s}$. Here C_s and C_w are the tracer concentrations in porous zone and fluid zone, respectively, $V_{ol,s}$ is the volume of the pore fluid [m^3], A_{SWI} is the area of the sediment-water interface [m^2]. Similar to the experimental results, the magnitude of the simulated V_H decreased for the first few minutes and then approached a constant value (Figure S16 in Supporting Information S1). Our simulation results show that as ϕ_v increased from 0 to 0.012 (Case Nos. S-F-01 to S-F-03 vs. Case Nos. S-S-01 to S-S-03 in Table 1), V_H increased by 9 times (Figure 9a). It is worth noting that V_H for the cases without vegetation in the simulations was twice as small as what was measured in the experiments (calculated based on the slopes of fitting lines in Figures 8a and 9a). This difference is likely because, in our simulations, the domains of the sediment and the surface water column were distinguished by the tag ζ_p. The additional turbulence and pressure gradient induced by the gravels protruding from the sediment bed were not considered. As a result, we anticipate that the hyporheic exchange in a channel with a flatbed was underestimated in the simulations. In addition, the dispersion coefficient is sensitive to various factors, which can easily lead to major differences in simulations and experiments. Furthermore, we applied a periodic boundary condition in the streamwise and spanwise directions for scalar transport modeling, which introduced an artificial recirculation of the solute. The re-entry of the solute in the streamwise direction caused an increase in the concentration of the solute in the surface flow, reduced the concentration gradient across the

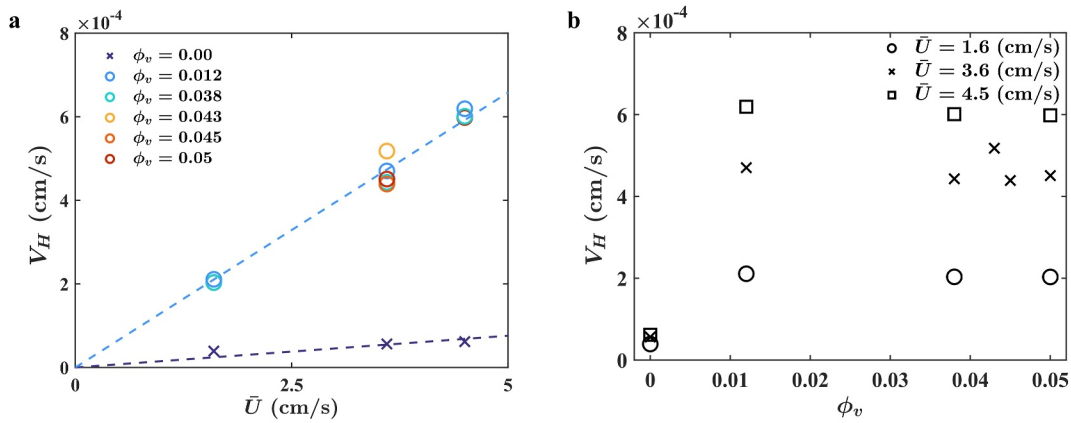

Figure 9. The simulated hyporheic exchange velocity V_H at different mean streamwise surface flow velocities $\overline{U}$ for cases with varying vegetation densities $\phi_v = 0, 0.012, 0.038, 0.043, 0.045$, and 0.05. (a) V_H is plotted against surface flow velocity. The crossmarks indicate cases without vegetation. The open circles indicate cases with vegetation. Color represents vegetation density ϕ_v. The dashed lines represent the linear regression lines of V_H on $\overline{U}$. The slopes for cases with and without vegetation were 1.32×10^{-4} and 0.15×10^{-4}, respectively. (b) V_H is plotted against vegetation density ϕ_v.

sediment-water interface, and resulted in an underprediction of tracer washout when compared to flume experiments. Despite the difference, the magnitude remains within the same order, and the trend is consistent. Considering the dispersion coefficients were not empirically tuned and the absence of other fitting parameters, the overall consistency between the experiments and simulations can be confirmed.

Also consistent with experiment results, our simulations showed that further increases in ϕ_v did not result in increases in V_H (Figure 9b). We conjecture that the independence of V_H on vegetation density is attributed to the combined effects of canopy-scale horizontal migration and stem-scale vertical flux on the total hyporheic exchange (Figure 6). These two effects have opposing dependencies on vegetation density and balance each other. Specifically, at the same mean flow velocity, as the vegetation density increases, the canopy-scale horizontal migration velocity increases due to the increasing drag force exerted by the vegetation stems, which induces larger pressure gradients in the streamwise direction (Huang & Yang, 2022). In contrast, as the vegetation density increases, the mean streamwise flow velocity gradient in the vertical direction decreases, causing peak upward vertical flow velocity $W_{\max}$ on the downstream side of the dowel to decrease (Figure S13b in Supporting Information S1), as noted by Nepf and Koch (1999). These two effects balance each other, which likely caused the total hyporheic exchange velocity to remain constant with increasing vegetation density. In previous studies, the hyporheic exchange processes used to be considered driven by a single factor. For example, the pressure gradient dominates hyporheic flows induced by bedform (Packman et al., 2004) and channel sinuosity (Cardenas, 2009), or the pressure perturbations created by the surface wave facilitate hyporheic exchange (Clark et al., 2019). Our results show that it could be important to consider the complex interaction between the flows at different scales to correctly predict hyporheic exchange in a vegetated channel. This information could also benefit the development of future theories to predict the exchange rate between the fast flow regions and the transient storage zone in transient storage models (Drummond et al., 2014; Knapp & Kelleher, 2020; Volponi et al., 2025).

Finally, we calculated the turbulent kinetic energy permeability Reynolds number $Re_{\mathrm{TKE}} = \sqrt{k}\sqrt{\mathrm{TKE}_{2\ \mathrm{cm}}}/\nu$ following Tseng and Tinoco (2022) for simulation cases (Case Nos. S-S-01 to S-S-03, S-M1-02, S-M2-01, S-M3-01, and S-D-01 to S-D-03 in Table 1). Here, $\mathrm{TKE}_{2\ \mathrm{cm}}$ is the turbulent kinetic energy 2 cm above the bed. The results are shown in Figure S17 in Supporting Information S1. The values of Re_{TKE} indicate that the exchange across the sediment-water interface in our simulations falls into the molecular and dispersion regimes according to the model proposed by Tseng and Tinoco (2022).

In summary, these results show that vegetation patches with density or volume fraction as low as $\phi_v = 0.012$ could enhance hyporheic exchange by 4 times. However, further increases in ϕ_v did not lead to additional increases in hyporheic exchange, suggesting that vegetation density as low as $\phi_v = 0.012$ is sufficient to induce hyporheic exchange similar to those induced by higher vegetation density. These findings will facilitate future restoration projects to design and evaluate the effectiveness of plant transplanting plan. Note that the above-

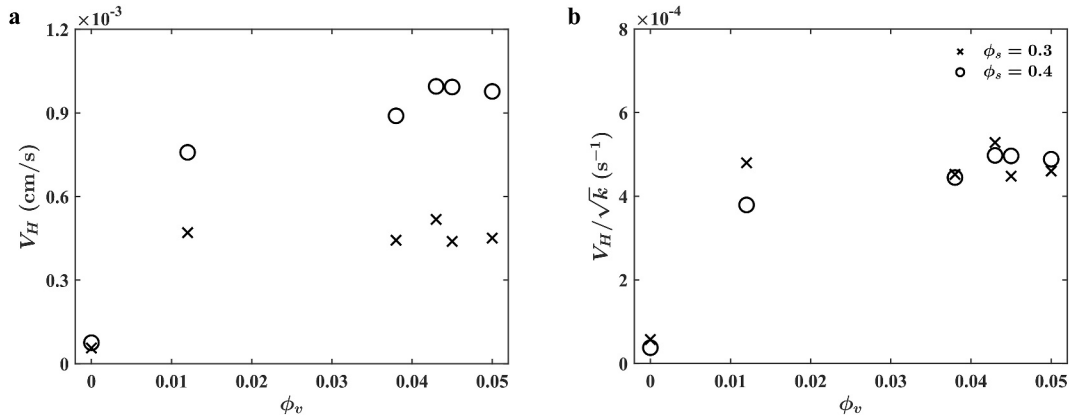

Figure 10. The simulated hyporheic exchange velocity V_H for cases with different sediment porosities. (a) V_H is plotted against vegetation density. (b) The simulated V_H normalized by the square root of sediment permeability $\sqrt{k}$ is plotted against vegetation density. The mean streamwise surface flow velocity was $\overline{U}$ = 3.6 cm/s for all the cases.

mentioned results were observed in a rigid-emergent vegetation canopy arranged in a staggered pattern. Whether our conclusion holds for different vegetation canopies, for example, flexible plants arranged in a random pattern, may be determined by the behaviors of the stem-scale vertical flows and canopy-scale horizontal migration in response to the vegetation density and requires further investigation.

3.4. Impact of Sediment Permeability on the Hyporheic Exchange

To further investigate the impact of sediment permeability on hyporheic exchange, we conducted simulations with two kinds of gravels. The sediment diameters were 6.0 and 5.6 mm, respectively. The porosities were ϕ_s = 0.4 and 0.3, respectively. The permeabilities of two gravels estimated using the Karman-Cozeny relationship were $k = \phi_s^3 d_s^2/180(1-\phi_s)^2 = 4.0 \times 10^{-2}$ and 9.6×10^{-3} mm^2, respectively (Voermans et al., 2018). For comparison, the mean streamwise surface flow velocity was kept constant at $\overline{U}$ = 3.6 cm/s for all cases (see the Methods section for details). Our results indicate that the hyporheic exchange velocity V_H in channels with a high permeable bed ($k = 4.0 \times 10^{-2}$ mm^2) was up to 1.6 times greater than in channels with a low permeable bed ($k = 9.6 \times 10^{-3}$ mm^2) across different vegetation densities (Figure 10a). The ratio between V_H normalized by the square root of the sediment permeability ($\sqrt{k}$) in the channels with two sediment permeabilities were 1.1 ± 0.2 across different vegetation densities, suggesting that V_H in a vegetated channel scaled with the square root of sediment permeability (Figure 10b). This finding is consistent with the previous studies focusing on parameterized interfacial exchange coefficients (Tseng & Tinoco, 2022; Voermans et al., 2018). Our results on the impact of vegetation on hyporheic exchange can potentially be applied to channels with a wider range of sediment permeability. However, in a channel with heterogeneous or biologically active sediments, the heterogeneity of the sediment may increase the hyporheic exchange rate (Salehin et al., 2004), and the biofilm could change the flow behaviors by changing the surface roughness (Volponi et al., 2025), which impacts on hyporheic exchange require further investigations.

4. Limitations of the Study and Future Works

While our integrated experimental and numerical approach provides key insights into vegetation-induced hyporheic exchange, we acknowledge limitations of the experiments and numerical model that offer avenues for future research.

For experiments, we used rigid acrylic dowels to simulate emergent vegetation. The impact of the flexibility of the plant on the flows is not considered. In addition, the vegetation dowels were placed in a staggered pattern in a homogenous sediment bed; the heterogeneity in the arrangement of the vegetation and in the sediment permeability on the hyporheic exchange were not considered. Finally, we did not include the biological activity in our experiments, which may impact the hyporheic exchange rate in a river and stream.

For simulations, the primary limitation is the use of a periodic boundary condition in the streamwise and spanwise directions for scalar transport modeling. While this boundary condition is appropriate for simulating the flow field across an infinite vegetation canopy, it introduces an artificial re-circulation of the solute. In our simulations, this re-entry in the streamwise direction leads to higher concentration of the solute in the surface flow when compared to that of the experimental setup. This, in turn, reduces the concentration gradient across the sediment-water interface and results in an underprediction of the tracer washout when compared to flume experiments (Figure S14 in Supporting Information S1). Second, the dispersion coefficients used in the porous media model were not empirically tuned. They were dynamically calculated from established theoretical models based on the local Peclet number. While this provides a robust, non-calibrated prediction, discrepancies between the idealized model and the complex dispersion in the experimental sediment bed can contribute to differences in the observed transport behavior.

To overcome these limitations, in addition to investigating complex vegetation and sediment conditions in experiments, future work will explore simulations in non-periodic domains that apply explicit inflow and outflow boundary conditions. This setup would facilitate a more straightforward quantitative comparison with solute transport metrics obtained from experimental studies. A second research direction will involve moving beyond the idealized flatbed of this study to investigate hyporheic exchange over porous beds with complex topography. We hypothesize that the increased turbulence generated by these topographies will lead to higher hyporheic exchange velocities, and future simulations will aim to quantify the contributions of different topological structures to the overall exchange process.

5. Conclusions

In this study, we combined index-matched flume experiments and fully-coupled numerical simulations to investigate the impact of emergent vegetation canopy on the hyporheic exchange in a channel with various vegetation densities, sediment permeabilities, and mean streamwise surface flow velocities. Our results indicate that the hyporheic exchange in a vegetation canopy was contributed by both stem-scale vertical flows around individual vegetation stems and canopy-scale horizontal flow within the sediment bed. In addition, we found that at the same mean streamwise surface flow velocity, the hyporheic exchange velocity V_H in a vegetated channel with $\phi_v = 0.012$ was 4 times higher than in a bare channel. However, further increases in ϕ_v did not lead to any increases in V_H, which may be due to the combined effects of canopy-scale horizontal migration and stem-scale vertical flux on the total hyporheic exchange. Furthermore, our results showed that V_H in channels with different sediment permeabilities (k) scaled with the square root of the sediment permeability ($\sqrt{k}$). While our findings can potentially be applied to predict hyporheic exchange in vegetated channels with varying vegetation densities and sediment permeabilities, how the factors that are not considered in this study, namely, the flexibility of the plant and the heterogeneity of the vegetation density and sediment permeability in natural settings, affect the phenomena we observed here is unclear. Further investigations in these areas could facilitate future designs of effective restoration projects involving vegetation.

Conflict of Interest

The authors declare no conflicts of interest relevant to this study.

Data Availability Statement

The raw data of the dye release experiments with a downward-looking camera has been deposited in The Data Repository for the University of Minnesota (Huang & Yang, 2021, https://doi.org/10.13020/W282-JJ11). The simulation data and data of the PIV measurements have been deposited on The Data Repository for the University of Minnesota (Huang et al., 2025, https://doi.org/10.13020/mc0f-wn59).

Acknowledgments
The research was supported by the National Science Foundation EAR 2209591.

References

Arenovski, A., & Howes, B. (1992). Lacunal allocation and gas transport capacity in the salt marsh grass Spartina alterniflora. *Oecologia*, *90*(3), 316–322. https://doi.org/10.1007/bf00317687

Aubeneau, A., Hanrahan, B., Bolster, D., & Tank, J. (2016). Biofilm growth in gravel bed streams controls solute residence time distributions. *Journal of Geophysical Research: Biogeosciences*, *121*(7), 1840–1850. https://doi.org/10.1002/2016jg003333

Bilbao-Ludena, J. C., & Papadakis, G. (2023). Structure of vorticity and turbulence fields in a separated flow around a finite wing: Analysis using direct numerical simulation. *Physical Review Fluids*, *8*(1), 014704. https://doi.org/10.1103/physrevfluids.8.014704

Boano, F., Demaria, A., Revelli, R., & Ridolfi, L. (2010). Biogeochemical zonation due to intrameander hyporheic flow. *Water Resources Research*, *46*(2), W02511. https://doi.org/10.1029/2008WR007583

Boano, F., Harvey, J. W., Marion, A., Packman, A. I., Revelli, R., Ridolfi, L., & Wörman, A. (2014). Hyporheic flow and transport processes: Mechanisms, models, and biogeochemical implications. *Reviews of Geophysics*, *52*(4), 603–679. https://doi.org/10.1002/2012rg000417

Bruneau, C. H., & Mortazavi, I. (2008). Numerical modelling and passive flow control using porous media. *Computers & Fluids*, *37*(5), 488–498. https://doi.org/10.1016/j.compfluid.2007.07.001

Cardenas, M. B. (2009). A model for lateral hyporheic flow based on valley slope and channel sinuosity. *Water Resources Research*, *45*(1), W01501. https://doi.org/10.1029/2008wr007442

Cardenas, M. B., & Wilson, J. L. (2007). Dunes, turbulent eddies, and interfacial exchange with permeable sediments. *Water Resources Research*, *43*(8), W08412. https://doi.org/10.1029/2006wr005787

Chandler, I., Guymer, I., Pearson, J., & Van Egmond, R. (2016). Vertical variation of mixing within porous sediment beds below turbulent flows. *Water Resources Research*, *52*(5), 3493–3509. https://doi.org/10.1002/2015wr018274

Cheng, N. S., & Nguyen, H. T. (2011). Hydraulic radius for evaluating resistance induced by simulated emergent vegetation in open-channel flows. *Journal of Hydraulic Engineering*, *137*(9), 995–1004. https://doi.org/10.1061/(asce)hy.1943-7900.0000377

Cimolin, F., & Discacciati, M. (2013). Navier–Stokes/Forchheimer models for filtration through porous media. *Applied Numerical Mathematics*, *72*, 205–224. https://doi.org/10.1016/j.apnum.2013.07.001

Clark, J. J., Qian, Q., Voller, V. R., & Stefan, H. G. (2019). Hyporheic exchange in a gravel bed flume with and without traveling surface waves. *Advances in Water Resources*, *123*, 120–133. https://doi.org/10.1016/j.advwatres.2018.11.005

Cui, Z., Yang, Z., Jiang, H. Z., Huang, W. X., & Shen, L. (2018). A sharp-interface immersed boundary method for simulating incompressible flows with arbitrarily deforming smooth boundaries. *International Journal of Computational Methods*, *15*(1), 1750080. https://doi.org/10.1142/s0219876217500803

Das, B. M. (2021). *Principles of geotechnical engineering*. Cengage Learning.

Delgado, J. (2007). Longitudinal and transverse dispersion in porous media. *Chemical Engineering Research and Design*, *85*(9), 1245–1252. https://doi.org/10.1205/cherd07017

D'Ippolito, A., Lauria, A., Alfonsi, G., & Calomino, F. (2019). Investigation of flow resistance exerted by rigid emergent vegetation in open channel. *Acta Geophysica*, *67*(3), 971–986. https://doi.org/10.1007/s11600-019-00280-8

Drummond, J., Aubeneau, A., & Packman, A. (2014). Stochastic modeling of fine particulate organic carbon dynamics in rivers. *Water Resources Research*, *50*(5), 4341–4356. https://doi.org/10.1002/2013wr014665

Dupuis, V., Proust, S., Berni, C., & Paquier, A. (2016). Combined effects of bed friction and emergent cylinder drag in open channel flow. *Environmental Fluid Mechanics*, *16*(6), 1173–1193. https://doi.org/10.1007/s10652-016-9471-2

Ghanbarian, B., Hunt, A. G., Ewing, R. P., & Sahimi, M. (2013). Tortuosity in porous media: A critical review. *Soil Science Society of America Journal*, *77*(5), 1461–1477. https://doi.org/10.2136/sssaj2012.0435

Grant, S. B., Stolzenbach, K., Azizian, M., Stewardson, M. J., Boano, F., & Bardini, L. (2014). First-order contaminant removal in the hyporheic zone of streams: Physical insights from a simple analytical model. *Environmental Science & Technology*, *48*(19), 11369–11378. https://doi.org/10.1021/es501694k

He, S. (2022). *Simulation of flexible stems and canopy flow with immersed boundary method (doctoral dissertation)*. University of Minnesota.

Hester, E. T., & Doyle, M. W. (2008). In-stream geomorphic structures as drivers of hyporheic exchange. *Water Resources Research*, *44*(3), W03417. https://doi.org/10.1029/2006WR005810

Huang, S. H., Nuli, R., & Yang, J. Q. (2025). Data for the flume experiments and numerical simulations of the surface and subsurface flows in an emergent vegetation canopy at St. Anthony Falls Laboratory in 2024 [Dataset]. https://doi.org/10.13020/mc0f-wn59

Huang, S. H., & Yang, J. Q. (2021). Experimental data of vegetation-induced hyporheic exchange experiment in Ecoflume of St. Anthony Falls laboratory on 2021 (29GB) [Dataset]. https://doi.org/10.13020/W282-JJ11

Huang, S. H., & Yang, J. Q. (2022). Impacts of emergent vegetation on hyporheic exchange. *Geophysical Research Letters*, *49*(13), e2022GL099095. https://doi.org/10.1029/2022gl099095

Huang, S. H., & Yang, J. Q. (2023). Impacts of channel-spanning log jams on hyporheic flow. *Water Resources Research*, *59*(11), e2023WR035217. https://doi.org/10.1029/2023wr035217

Iliev, O., & Laptev, V. (2004). On numerical simulation of flow through oil filters. *Computing and Visualization in Science*, *6*(2–3), 139–146. https://doi.org/10.1007/s00791-003-0118-8

Jin, G., Zhang, S., Zhou, B., Yang, Y., Zhang, Z., Chen, H., & Tang, H. (2023). Solute transport characteristics in the streambed due to rigid non-submerged plants: Experiment and simulations. *Journal of Hydrology*, *619*, 129315. https://doi.org/10.1016/j.jhydrol.2023.129315

Kim, J., & Moin, P. (1985). Application of a fractional-step method to incompressible Navier-Stokes equations. *Journal of Computational Physics*, *59*(2), 308–323. https://doi.org/10.1016/0021-9991(85)90148-2

Kitsikoudis, V., Yagci, O., & Kirca, V. S. O. (2020). Experimental analysis of flow and turbulence in the wake of neighboring emergent vegetation patches with different densities. *Environmental Fluid Mechanics*, *20*(6), 1417–1439. https://doi.org/10.1007/s10652-020-09746-6

Knapp, J. L., & Kelleher, C. (2020). A perspective on the future of transient storage modeling: Let's stop chasing our tails. *Water Resources Research*, *56*(3), e2019WR026257. https://doi.org/10.1029/2019wr026257

Lanfrey, P. Y., Kuzeljevic, Z. V., & Dudukovic, M. P. (2010). Tortuosity model for fixed beds randomly packed with identical particles. *Chemical Engineering Science*, *65*(5), 1891–1896. https://doi.org/10.1016/j.ces.2009.11.011

Li, A., Aubeneau, A. F., Bolster, D., Tank, J. L., & Packman, A. I. (2017). Covariation in patterns of turbulence-driven hyporheic flow and denitrification enhances reach-scale nitrogen removal. *Water Resources Research*, *53*(8), 6927–6944. https://doi.org/10.1002/2016wr019949

Liu, C., & Nepf, H. (2016). Sediment deposition within and around a finite patch of model vegetation over a range of channel velocity. *Water Resources Research*, *52*(1), 600–612. https://doi.org/10.1002/2015wr018249

Liu, D., Diplas, P., Fairbanks, J., & Hodges, C. (2008). An experimental study of flow through rigid vegetation. *Journal of Geophysical Research*, *113*(F4), F04015. https://doi.org/10.1029/2008JF001042

Lv, J., Gao, X., & Sun, B. (2022). Numerical simulation of hyporheic exchange driven by an emergent vegetation patch. *Hydrological Processes*, *36*(11), e14756. https://doi.org/10.1002/hyp.14756

Marion, A., Bellinello, M., Guymer, I., & Packman, A. (2002). Effect of bed form geometry on the penetration of nonreactive solutes into a streambed. *Water Resources Research*, *38*(10), 1209. https://doi.org/10.1029/2001WR000264

McCallum, J. L., Höhne, A., Schaper, J. L., Shanafield, M., Banks, E. W., Posselt, M., et al. (2020). A numerical stream transport modeling approach including multiple conceptualizations of hyporheic exchange and spatial variability to assess contaminant removal. *Water Resources Research*, *56*(3), e2019WR024987. https://doi.org/10.1029/2019wr024987

Mueller, B. M., Schulz, H., Danczak, R. E., Putschew, A., & Lewandowski, J. (2021). Simultaneous attenuation of trace organics and change in organic matter composition in the hyporheic zone of urban streams. *Scientific Reports*, *11*(1), 1–13. https://doi.org/10.1038/s41598-021-83750-8

Nepf, H. M. (1999). Drag, turbulence, and diffusion in flow through emergent vegetation. *Water Resources Research*, *35*(2), 479–489. https://doi.org/10.1029/1998wr900069

Nepf, H. M. (2012). Flow and transport in regions with aquatic vegetation. *Annual Review of Fluid Mechanics*, *44*(1), 123–142. https://doi.org/10.1146/annurev-fluid-120710-101048

Nepf, H. M., & Koch, E. W. K. (1999). Vertical secondary flows in submersed plant-like arrays. *Limnology & Oceanography*, *44*(4), 1072–1080. https://doi.org/10.4319/lo.1999.44.4.1072

Neumeier, U. (2007). Velocity and turbulence variations at the edge of saltmarshes. *Continental Shelf Research*, *27*(8), 1046–1059. https://doi.org/10.1016/j.csr.2005.07.009

Nguyen, V., & Papavassiliou, D. V. (2020). Hydrodynamic dispersion in porous media and the significance of Lagrangian time and space scales. *Fluid*, *5*(2), 79. https://doi.org/10.3390/fluids5020079

O'Connor, B. L., & Harvey, J. W. (2008). Scaling hyporheic exchange and its influence on biogeochemical reactions in aquatic ecosystems. *Water Resources Research*, *44*(12), W12423. https://doi.org/10.1029/2008wr007160

O'Connor, B. L., & Hondzo, M. (2008). Dissolved oxygen transfer to sediments by sweep and eject motions in aquatic environments. *Limnology & Oceanography*, *53*(2), 566–578. https://doi.org/10.4319/lo.2008.53.2.0566

Packman, A. I., Salehin, M., & Zaramella, M. (2004). Hyporheic exchange with gravel beds: Basic hydrodynamic interactions and bedform-induced advective flows. *Journal of Hydraulic Engineering*, *130*(7), 647–656. https://doi.org/10.1061/(asce)0733-9429(2004)130:7(647)

Raffel, M., Willert, C. E., Scarano, F., Kähler, C. J., Wereley, S. T., & Kompenhans, J. (2018). *Particle image velocimetry: A practical guide*. Springer.

Roche, K. R., Shogren, A. J., Aubeneau, A., Tank, J. L., & Bolster, D. (2019). Modeling benthic versus hyporheic nutrient uptake in unshaded streams with varying substrates. *Journal of Geophysical Research: Biogeosciences*, *124*(2), 367–383. https://doi.org/10.1029/2018jg004684

Rominger, J. T., & Nepf, H. M. (2011). Flow adjustment and interior flow associated with a rectangular porous obstruction. *Journal of Fluid Mechanics*, *680*, 636–659. https://doi.org/10.1017/jfm.2011.199

Salehin, M., Packman, A. I., & Paradis, M. (2004). Hyporheic exchange with heterogeneous streambeds: Laboratory experiments and modeling. *Water Resources Research*, *40*(11), W11504. https://doi.org/10.1029/2003wr002567

Schaper, J. L., Posselt, M., Bouchez, C., Jaeger, A., Nuetzmann, G., Putschew, A., et al. (2019). Fate of trace organic compounds in the hyporheic zone: Influence of retardation, the benthic biolayer, and organic carbon. *Environmental Science & Technology*, *53*(8), 4224–4234. https://doi.org/10.1021/acs.est.8b06231

Stoesser, T., Kim, S., & Diplas, P. (2010). Turbulent flow through idealized emergent vegetation. *Journal of Hydraulic Engineering*, *136*(12), 1003–1017. https://doi.org/10.1061/(asce)hy.1943-7900.0000153

Stonedahl, S. H., Harvey, J. W., Wörman, A., Salehin, M., & Packman, A. I. (2010). A multiscale model for integrating hyporheic exchange from ripples to meanders. *Water Resources Research*, *46*(12), W12539. https://doi.org/10.1029/2009WR008865

Sumner, D., Heseltine, J. L., & Dansereau, O. J. P. (2004). Wake structure of a finite circular cylinder of small aspect ratio. *Experiments in Fluids*, *37*(5), 720–730. https://doi.org/10.1007/s00348-004-0862-7

Tanino, Y., & Nepf, H. M. (2008). Lateral dispersion in random cylinder arrays at high Reynolds number. *Journal of Fluid Mechanics*, *600*, 339–371. https://doi.org/10.1017/s0022112008000505

Thielicke, W., & Sonntag, R. (2021). Particle Image Velocimetry for MATLAB: Accuracy and enhanced algorithms in PIVlab. *Journal of Open Research Software*, *9*(1), 12. https://doi.org/10.5334/jors.334

Tonina, D., & Buffington, J. M. (2009). Hyporheic exchange in Mountain Rivers I: Mechanics and environmental effects. *Geography Compass*, *3*(3), 1063–1086. https://doi.org/10.1111/j.1749-8198.2009.00226.x

Tseng, C. Y., & Tinoco, R. O. (2021). A two-layer turbulence-based model to predict suspended sediment concentration in flows with aquatic vegetation. *Geophysical Research Letters*, *48*(3), e2020GL091255. https://doi.org/10.1029/2020GL091255

Tseng, C. Y., & Tinoco, R. O. (2022). From substrate to surface: A turbulence-based model for gas transfer across sediment-water-air interfaces in vegetated streams. *Water Resources Research*, *58*(1), e2021WR030776. https://doi.org/10.1029/2021wr030776

Ullah, S., Zhang, H., Heathwaite, A. L., Heppell, C., Lansdown, K., Binley, A., & Trimmer, M. (2014). Influence of emergent vegetation on nitrate cycling in sediments of a groundwater-fed river. *Biogeochemistry*, *118*(1–3), 121–134. https://doi.org/10.1007/s10533-013-9909-2

Voermans, J. J., Ghisalberti, M., & Ivey, G. N. (2018). A model for mass transport across the sediment-water interface. *Water Resources Research*, *54*(4), 2799–2812. https://doi.org/10.1002/2017wr022418

Volponi, S. N., Tank, J. L., Vincent, A. E., Snyder, E. D., Pruitt, A. N., & Bolster, D. (2025). Biofilm development, senescence, and benthic substrate influence hyporheic transport in streams. *Journal of Geophysical Research: Biogeosciences*, *130*(2), e2024JG008225. https://doi.org/10.1029/2024jg008225

Waterman, B., & Hansen, A. (2024). Hydro-biogeochemical controls on nitrate removal: Insights from artificial emergent vegetation experiments in a recirculating flume mesocosm. *Water Resources Research*, *60*(8), e2023WR036995. https://doi.org/10.1029/2023wr036995

Xia, Y., Zhang, M., Tsang, D. C., Geng, N., Lu, D., Zhu, L., et al. (2020). Recent advances in control technologies for non-point source pollution with nitrogen and phosphorous from agricultural runoff: Current practices and future prospects. *Applied Biological Chemistry*, *63*, 1–13. https://doi.org/10.1186/s13765-020-0493-6

Xu, Y., & Nepf, H. (2020). Measured and predicted turbulent kinetic energy in flow through emergent vegetation with real plant morphology. *Water Resources Research*, *56*(12), e2020WR027892. https://doi.org/10.1029/2020wr027892

Yang, J. Q. (2024). Solute flow and particle transport in aquatic ecosystems: A review on the effect of emergent and rigid vegetation. *Environmental Science & Ecotechnology*, *21*, 100429. https://doi.org/10.1016/j.ese.2024.100429

Yang, J. Q., Chung, H., & Nepf, H. M. (2016). The onset of sediment transport in vegetated channels predicted by turbulent kinetic energy. *Geophysical Research Letters*, *43*(21), 11261–11268. https://doi.org/10.1002/2016gl071092

Yang, J. Q., Kerger, F., & Nepf, H. M. (2015). Estimation of the bed shear stress in vegetated and bare channels with smooth beds. *Water Resources Research*, *51*(5), 3647–3663. https://doi.org/10.1002/2014wr016042

Yeung, P.-K., & Pope, S. B. (1989). Lagrangian statistics from direct numerical simulations of isotropic turbulence. *Journal of Fluid Mechanics*, *207*, 531–586. https://doi.org/10.1017/s0022112089002697

Yuan, Y., Chen, X., Cardenas, M. B., Liu, X., & Chen, L. (2021). Hyporheic exchange driven by submerged rigid vegetation: A modeling study. *Water Resources Research*, *57*(6), e2019WR026675. https://doi.org/10.1029/2019wr026675